

No.: egusphere-2024-2869

Title: Measurement report: Crustal materials play an increasing role in elevating particle pH: Insights from 12-year records in a typical inland city of China.

Reviewer #2:

General Comments:

Zhang et al. analyzed the particle pH collected in a Chinese inland city. This analysis is based on 4228 filter samples collected from four seasons in 2011 – 2022. As a measurement report, the study fits into the scope of Atmospheric Chemistry and Physics. The authors claim that the evolving particle pH was driven by the interplay of declines in SO_4^{2-} , increases in TNH_x , and rises in Ca^{2+} concentrations over time. The manuscript can be considered for publication once the comments below are addressed.

Thank you for your careful reading of our paper and valuable comments and suggestions. We believe that we have adequately addressed your comments. To facilitate your review, we used green highlights for your comments, yellow highlights for Reviewer #1, and red color indicating our own corrections in the manuscript.

Major Comment:

1. lines 111-112 and 120–121: It is unclear whether Ti was measured or not.

Response: Sorry for the mistake. We did not measure the element Ti. The sentence has been corrected:

“Elements were analyzed using a wavelength dispersive X-ray fluorescence spectrometer (S8 TIGER,

Bruker, Germany) to determine concentrations of Fe, Na, Mg, Al, Si, Cl, K, Ca, V, Ni, Cu, Zn, Cr, Mn, Co, Cd, Ga, As, Se, Sr, Sn, Sb, Ba, and Pb (Tremper et al., 2018).”

2. Lines 135 – 136: The linear regression proposed by Wei et al. (2023) is based on the dataset collected in the wintertime but not from 2013 to 2020. This needs clarification. Since the regression was based on wintertime data, it is questionable if the relationship is still valid for data in seasons other than winter.

Response: Thanks for your comment. We have added a validation of the simulated NH₃: “To validate the applicability of Equation 4 for annual NH₃ estimation and pH simulation in Zhengzhou, this study utilized both observed NH₃ data (from a Thermo Scientific URG-9000D ambient ion monitor, USA) and calculated NH₃ values derived from Equation 4 at the same monitoring site throughout 2022, inputting them into the thermodynamic model for pH simulation. As shown in Figure S2, pH values calculated from observed and simulated NH₃ exhibit good agreement ($r = 0.97$, $P < 0.01$). Furthermore, NH₃ concentrations modeled by ISORROPIA demonstrate a significant correlation ($r = 0.95$, $P < 0.01$) with that simulated NH₃ by Equation 4. These results collectively demonstrate the reliability of the NH₃ estimation method in this study.”

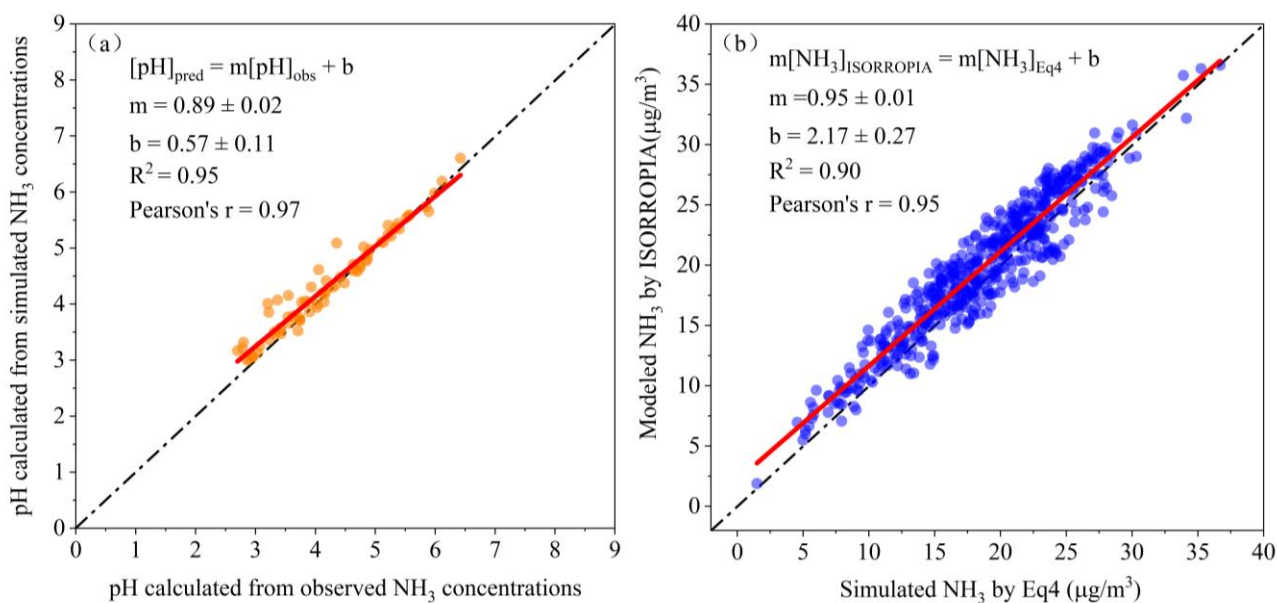


Figure S2. Verification of the NH₃ Method.

3. Section 2.2.3: Why was 1000 m chosen as the height in the HYSPLIT simulations? If 1000 m was already well above the boundary layer height, how do the simulated back trajectory simulations represent the ground-level measurements? In addition, how was the optimum number of clusters chosen by the authors? What clustering technique was used in the analysis? What data was used as the meteorological input?

Response: Thanks for your comments.

While the surface elevation of Zhengzhou is approximately 100 m above sea level (ASL), setting the height at 1000 m ASL takes into account the minimum altitude needed to traverse the average elevation of the Taihang Mountains (ranging from 1000 to 1500 m ASL). This ensures that the simulated trajectory paths over this topographical barrier are physically realistic.

The Angle Distance algorithm was used to cluster air mass trajectories, enabling the identification of dominant air mass directions and potential pollution sources affecting the study site during different periods. The optimal number of clusters was determined by evaluating the spatial variance (SPVAR)

of each trajectory from the cluster mean and the total spatial variance (TSV). The final classification was selected just before the second rapid increase in TSV. The underlying principle is that TSV initially rises sharply during clustering, then increases gradually; however, once the number of clusters reaches a certain threshold, TSV surges again, indicating that the merged clusters are highly dissimilar, marking the end of the classification process. The classification results correspond to the different air mass categories before this final merging step. The mean trajectories of these clusters represent the primary airflow patterns at the target site during the analysis period (Wang et al., 2009).

The HYSPLIT simulations utilized meteorological input data from the Global Data Assimilation System (GDAS) with 3D wind vectors, temperature, relative humidity, geopotential height, surface pressure, and boundary layer diagnostics.

In the revised version, these descriptions have been added in Section 2.2.3:

“Backward trajectories were calculated using the mixed-particle Lagrangian integrated trajectory method (HYSPLIT, https://www.ready.noaa.gov/HYSPLIT_traj.php). Meteorological input data were from the Global Data Assimilation System (GDAS) with 3D wind vectors, temperature, relative humidity, geopotential height, surface pressure, and boundary layer diagnostics. 24-h backward trajectories were simulated for air masses above 1000 m above ground level in Zhengzhou. While the surface elevation of Zhengzhou is approximately 100 m above sea level (ASL), setting the height at 1000 m ASL takes into account the minimum altitude needed to traverse the average elevation of the Taihang Mountains (ranging from 1000 to 1500 m ASL). This ensures that the simulated trajectory paths over this topographical barrier are physically realistic.

The Angle Distance algorithm was used to cluster air mass trajectories, enabling the identification

of dominant air mass directions and potential pollution sources affecting the study site during different periods. The optimal number of clusters was determined by evaluating the spatial variance (SPVAR) of each trajectory from the cluster mean and the total spatial variance (TSV). The final classification was selected just before the second rapid increase in TSV. The underlying principle is that TSV initially rises sharply during clustering, then increases gradually; however, once the number of clusters reaches a certain threshold, TSV surges again, indicating that the merged clusters are highly dissimilar, marking the end of the classification process. The classification results correspond to the different air mass categories before this final merging step. The mean trajectories of these clusters represent the primary airflow patterns at the target site during the analysis period (Wang et al., 2009). Subsequently, trajectories from two periods, 2013–2018 and 2019–2022, were clustered separately to analyze the variations between the two policy implementation periods.”

4. Sections 3.1 and 3.2: How did the author estimate the decreases in the mass concentrations? Which year was chosen as the reference year? A proper analysis using Mann-Kendall and Sen’s slope should be carried out here and in other places associated with trend analysis.

Response: Thank you for your comment. In the revised manuscript, the Mann - Kendall, Sen’s slope, and Least - Squares slope methods were comprehensively used to analyze the inter - annual change trends. Please refer to Table S4 for details.

Table S4. Analysis of the inter - annual trends of CM and Ca²⁺ concentrations and pH during different periods using multiple methods.

	2011–2013			2013–2019			2019–2022		
	CM	Ca ²⁺	pH	CM	Ca ²⁺	pH	CM	Ca ²⁺	pH
MK-Z	3.01	2.70	1.41	−9.74	−13.62	3.00	2.48	8.21	5.12
MK- <i>p</i>	0.003	0.007	0.159	<2.2 E−16	<2.2E−16	0.003	0.013	2.20E−16	2.99E−07
Sen's slope	0.082	0.023	7.10E−03	−0.015	−4.14E−03	9.15E−04	5.80E−03	5.42E−03	2.93E−03
LS slope	2.65	0.61	/	−0.81	−0.32	0.11	0.24	0.40	0.21

** MK-Z and MK-*p* represent the trend (Z) and significance (*p*) calculated by the Mann - Kendall method using daily data, respectively; Sen's

slope represents the Sen slope using daily data; LS slope represents the Least - Squares slope using annual data. All the above calculations were

performed using the R language (R version 4.0.2).

5. Please briefly describe the Air Pollution Prevention and Control Action Plan and Three-Year Action Plan in the main text. In general, readers outside China have no idea about these policies.

Response: Thank you for your comments. We have added a description of the policies: “Over the past twelve years, the Chinese government implemented the Air Pollution Prevention and Control Action Plans (2013–2018) and the Three-Year Action Plan (2018–2020). The Air Pollution Prevention and Control Action Plan focused on reducing PM_{2.5} concentrations in key regions and aiming to cut PM_{2.5} levels by 10–25% in priority areas over five years. To achieve these goals, it adopted several measures. In terms of industrial restructuring, it mandated the elimination of a large amount of outdated production capacity in industries such as iron/steel and cement to optimize the industrial structure and reduce high-pollution production. For emission standards, it set strict requirements for multiple industrial sectors, especially coal-fired power plants, and gradually introduced ultra-low emission requirements to control pollutants like SO₂, NO_x, and PM. Regarding energy transition, it promoted a shift from coal to cleaner energy sources, including capping coal consumption in certain regions and restricting the construction of small-scale coal-fired boilers. Subsequently, the Three-Year Action Plan was carried out to continue improving air quality with a broader scope of regions under control, further reducing pollutant emissions and enhancing the overall air quality index. The measures included enhanced transportation controls, such as introducing stricter vehicle emission standards (like National VI standards for vehicles) and establishing diesel truck exclusion zones in many cities to reduce emissions from the transportation sector. It also adopted precision governance through grid-based environmental supervision, dividing areas into small grids for more accurate and efficient monitoring of pollution sources. Additionally, it strengthened the legal and institutional framework by revising

relevant laws, such as the Air Pollution Prevention and Control Law, to strengthen legal penalties for environmental violations and implementing an environmental tax system to encourage enterprises to reduce emissions. Correspondingly, the annual average concentration of PM_{2.5} in Zhengzhou decreased from $212 \pm 102 \text{ } \mu\text{g}/\text{m}^3$ in 2013 to $60 \pm 41 \text{ } \mu\text{g}/\text{m}^3$ in 2022, representing a reduction of approximately 72%.”

6. Please explain why Zhengzhou is representative of a typical inland city in North China in the main text. There is no background information about aerosol research conducted in Zhengzhou and how they compare with those findings in other typical Chinese megacities, such as Beijing or Shanghai.

Response: Thanks for your comment. We have added a summary section:

“Zhengzhou presents unique atmospheric chemistry that distinguishes it from other mega-cities in North China. As the capital of China’s foremost agricultural province (Henan Province, contributing 18% of national NH₃ emissions), Zhengzhou’s PM_{2.5} composition combined substantial crustal material ($15 \pm 3\%$ in PM_{2.5} vs. $<10\%$ in Beijing) with exceptional ammonia abundance (Huang et al., 2012; Liu et al., 2018; Wang et al., 2018). This created distinct particle acidity characteristics, maintaining pH 4.5–6.0 compared to lower pH levels (3.3–5.4) in other cities like Beijing (Ding et al., 2019; Zhang et al., 2021). However, two critical research gaps persist: (1) the long-term evolution of CM under control policies remains unquantified; (2) the role of CM on pH buffer capacity in NH₃-enriched environments lacks systematic assessment.

To address these gaps, our study pioneers the first multi-decadal analysis (2011–2022) coupling PM_{2.5} components with thermodynamic modeling through three key innovations: (1) revealing the long-term trends of CM, (2) analyzing the variations of CM sources, and (3) exploring pH trend and

its relationship with CM. The resultant findings advance our understanding of urban aerosol acidity chemistry by underscoring the critical role of CM.”

Minor Comment:

1. Figure S1: Please label the highways, coal-fired power plants, and gas-fired power plants on the map.

Response: Thanks for your comment. We have updated Figure S1:

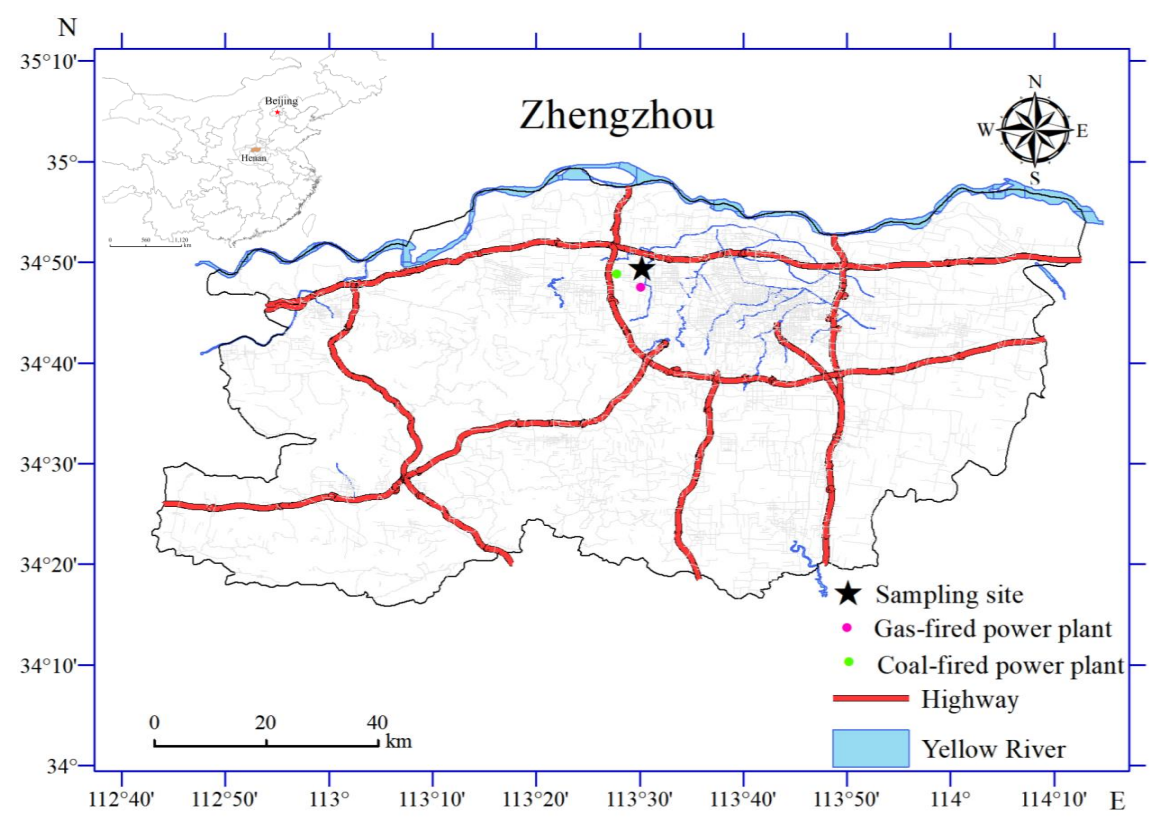


Figure S1. Sampling site in Zhengzhou, China. © 2019 National Geomatics Center of China. All rights reserved.

2. Section 2.1: What are the uncertainties in the measured concentrations for individual components?

Response: Thanks for your comment. The method detection limits and measurement uncertainties are summarized in Table S2.

Table S2 The method detection limit (MDL) and measurement uncertainties (Unc) of individual

components		
	MDLs ($\mu\text{g}/\text{m}^3$)	Unc (%)
EC	0.1	13.1
OC	0.1	9.8
Na ⁺	0.005	9.6
NH ₄ ⁺	0.011	10.1
K ⁺	0.006	9.5
Mg ²⁺	0.002	9.3
Ca ²⁺	0.017	8.8
F ⁻	0.001	8.2
Cl ⁻	0.001	9.3
NO ₃ ⁻	0.015	10.1
SO ₄ ²⁻	0.031	9.9
Na	0.003	10.9
Mg	0.002	10.6
Al	0.004	9.2
Si	0.005	9.3
Cl	0.008	9.5
K	0.005	9.4
Ca	0.01	9.4
V	0.008	57.9
Ni	0.006	96.6
Cr	0.02	24.7
Mn	0.02	16.8
Fe	0.03	9.3
Co	0.009	79.6
Cu	0.005	5.8
Zn	0.003	8.4
Ga	0.005	84.7
As	0.008	27.4
Se	0.006	25.7
Sr	0.006	22.8
Cd	0.03	68.6
Sn	0.02	42.0
Sb	0.02	73.6
Ba	0.02	15.6
Pb	0.02	13.4

3. Lines 114 – 115: Apart from just citing references here, please provide the details about analytical methods and quality control in the supplement.

Response: Thanks for your comments. We have added detailed analytical methods and quality control in both the Manuscript and Supplement material:

Manuscript

“Blank filters were also routinely analyzed with each batch of samples to detect sample contamination and provide quality assurance on the elemental concentrations. Detailed analytical methods and quality control are described in the supplement (Text S1). The method detection limits and measurement uncertainties are summarized in Table S2.”

Supplement material

“Text S1 Instruments and Measurements

Samples were collected using a high-volume sampler (TE-6070D, Tisch, USA) and air particulate samplers (TH-16A, Tianhong, China) from April 2011 to December 2022. Two quartz filters and two Teflon filters were used daily from 10:00 AM to 9:00 AM the next day, resulting in a total of 5848 samples. After excluding abnormal data due to instrument malfunctions, 4228 valid samples were obtained. Detailed information on the samples is provided in Table S1.

Organic carbon (OC) and elemental carbon (EC) were analyzed using a carbon analyzer (Model 5L, Sunset Laboratory, USA). The analysis of EC and OC was conducted in two stages. In the first stage, the filter membrane was placed in a quartz heating furnace under a pure helium atmosphere. As the temperature gradually increased to approximately 580°C, OC was volatilized and released. In the second stage, heating continued in a mixed atmosphere of 2% oxygen and 98% helium. When the temperature reached approximately 870°C, EC underwent oxidative decomposition and was released.

During the helium flow transmission, OC and EC released at different temperatures were completely oxidized to CO₂ in a MnO₂ oxidation furnace and subsequently reduced to CH₄ for detection by a flame ionization detector (FID). The detection limits for both OC and EC were 0.2 µg/cm². Before each sample analysis, calibration was performed using a standard sucrose solution. Additionally, parallel tests were conducted every ten samples to ensure accuracy.

Water-soluble inorganic ions (Cl⁻, NO₃⁻, SO₄²⁻, Na⁺, NH₄⁺, K⁺, Mg²⁺, and Ca²⁺) were measured using ion chromatography (ICS-90 and ICS-900 models, Dionex, USA). Half of the PM_{2.5} filter was cut into pieces and ultrasonically extracted with 20 mL of Milli-Q water for 30 min, followed by filtering through a 0.45 mm polytetrafluoroethylene syringe filter before analysis. The cation concentrations were determined by an IonPacASII-HC4 mm anion separation column and an IonPacAGII-HC4 mm guard column, with 20 mM methane sulfonate as an eluent at 0.8 mL/min. The anions were measured by an IonPacCS12A cation separation column and an IonPacCG12A guard column, with a solution of 8.0 mM Na₂CO₃ + 1.0 mM NaHCO₃ as an eluent at 1.0 mL/min. The regression coefficients (R²) of the calibration curves were over 0.9996 for all ions, except NH₄⁺ (0.9988), which showed a quadratic response.

Elements were analyzed using a wavelength dispersive X-ray fluorescence spectrometer (S8 TIGER, Bruker, Germany) to determine concentrations of Fe, Na, Mg, Al, Si, Cl, K, Ca, V, Ni, Cu, Zn, Cr, Mn, Co, Cd, Ga, As, Se, Sr, Sn, Sb, Ba, and Pb (Tremper et al., 2018), which has been approved by the United States Environmental Protection Agency (Chow and Watson, 1994). The spectrometer was equipped with an X-ray tube featuring close coupling among the tube, sample, and detector, ensuring high efficiency and optimal excitation of elements within the sample. Before analysis, the instrument was calibrated using a series of high-quality, self-prepared standards. Calibration

procedures were conducted following established methods (Chow and Watson, 1994). To assess potential contamination and ensure data quality, blank filters were routinely analyzed alongside each batch of samples.”

4. Section 2.2.2: What was the set activity coefficient of H in the model?

Response: With ISORROPIA, γ_{H^+} and γ_{OH^-} are assumed to be equal to unity, whereas the activity coefficients for the other ionic pairs (e.g., H^+-Cl^-) are calculated by Kusik-Meissner method (Fountoukis and Nenes, 2007).

Fountoukis, C. and Nenes, A.: ISORROPIA II: a computationally efficient thermodynamic equilibrium model for $K^+-Ca^{2+}-Mg^{2+}-NH_4^+-Na^+-SO_4^{2-}-NO_3^- -Cl^- -H_2O$ aerosols, Atmos. Chem. Phys., 7, 4639–4659, <https://doi.org/10.5194/acp-7-4639-2007>, 2007.

5. Line 172: There is no data showing that the WS was higher in spring and summer compared to autumn and winter.

Response: According to the comments of Reviewer 1, this part has been revised to:

“Seasonal trends (Fig. S5) reveal significant declines in CM during spring in 2013–2019 with WS decreasing from 2.2 m/s in 2013 to 1.4 m/s in 2019 (Fig. S6) and stable RH (Fig. S7). Similarly, summer CM reductions in 2013–2019 corresponded with WS declines. These patterns suggest spring-summer CM improvements resulted from the synergistic effects of meteorological changes and dust control policies. Conversely, autumn-winter seasons showed limited CM reductions despite comparable WS decreases in 2013–2019, highlighting the need for enhanced dust emission controls in

Zhengzhou during these seasons.”

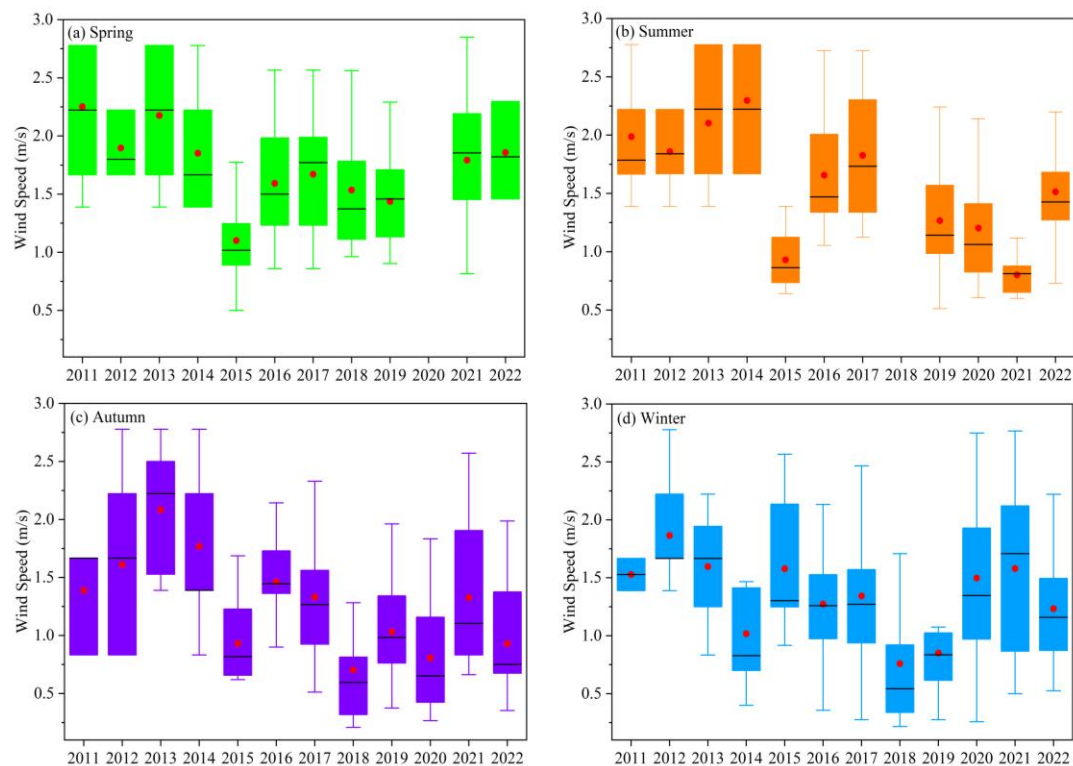


Figure S6 The variation in WS across different seasons from 2011 to 2022.

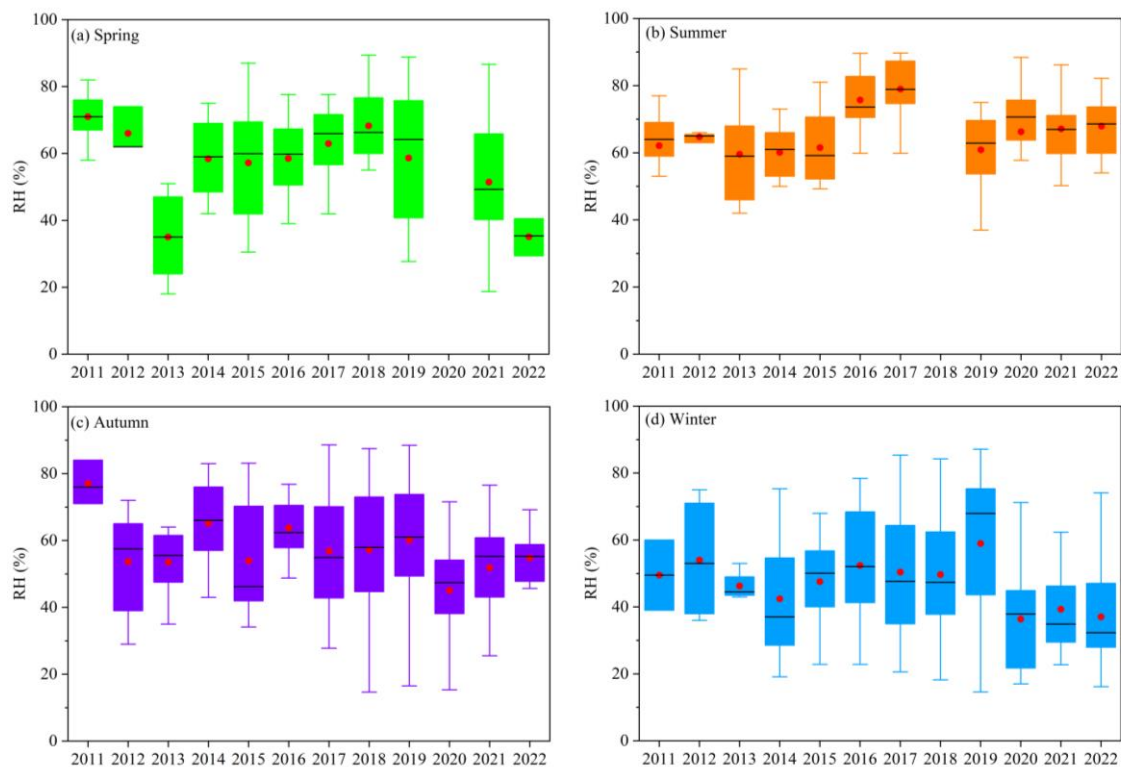


Figure S7 The variation in RH across different seasons from 2011 to 2022.

6. Figure S4: Is there any data for Ca^{2+} in 2015?

Response: Thank you for your comments. The relevant data for Ca^{2+} has been presented in Figure 2 of the main text.

7. Lines 229 – 231: Please provide a discussion about why the pH trend is similar to those in Beijing but different from those in Shanghai and Hong Kong.

Response: Thanks for your suggestion. We have added a discussion: “The increasing trend in pH values observed in this study is similar to the findings in Beijing (Song et al., 2019; Xie et al., 2020), presumably attributable to the comparable chemical composition trends and meteorological conditions. In contrast, Shanghai and Hong Kong display divergent trends (Nah et al., 2023; Zhou et al., 2022). This disparity might be ascribed to the stronger buffering effect exerted by NH_3 and dust in Zhengzhou than marine aerosols (Na^+/Cl^-) in these coastal cities (Shi et al., 2017; Liu et al., 2019). Moreover, the relatively higher temperatures and more abundant rainfall in Shanghai and Hong Kong could also contribute to the distinct trends observed in their pH values.”

8. Figure 5: How did the authors estimate the contribution of a component to the changes in pH?

Response: First, we conducted a sensitivity analysis using all the observational data from 2011 to 2022. A given range for a variable (i.e., TNHx) along with the corresponding average values of other parameters (i.e., SO_4^{2-} , NO_3^- , Na^+ , Cl^- , Ca^{2+} , K^+ , Mg^{2+} , RH, and T) was input into ISORROPIA-II to investigate the sensitivity of particle pH to this variable (i.e., TNHx), and the results are presented in

Fig. S10 in the Supplement. Based on the sensitivity analysis curves, the pH values corresponding to a variable in different years were calculated according to the average values of this variable in different years (Table S6). The difference in pH values of this variable between two adjacent years was defined as ΔpH . The above description has also been added to the main text:

“Sensitivity analyses were conducted to explore the dominant factors driving the elevated particle pH in Zhengzhou by giving a range for one parameter (i.e., TNHx) and average values for other parameters (i.e., SO_4^{2-} , NO_3^- , Na^+ , Cl^- , Ca^{2+} , K^+ , Mg^{2+} , RH, and T) input into the ISORROPIA-II model.”

“Based on the sensitivity analysis curves, the pH values corresponding to a variable in different years were calculated according to the average values of this variable in different years (Table S6). The difference in pH values of this variable between two adjacent years was defined as ΔpH which is illustrated in Fig. 5”

9. Where is the figure or table associated with Lines 256 – 266?

Response: Sorry for the misunderstanding. This sentence has been modified to: “During the period from 2020 to 2022, the influence of SO_4^{2-} on particle pH gradually decreased, with a decrease in concentration from 0.3 to 2.3 $\mu\text{g}/\text{m}^3$ (Table S6) only bringing about a pH decrease of 0.03 to 0.14 (Fig. 5).

Technical Comment:

1. Line 17: It is unclear what is "particle pH response"

Response: Thank you for your careful reading of our paper. We have implemented the following

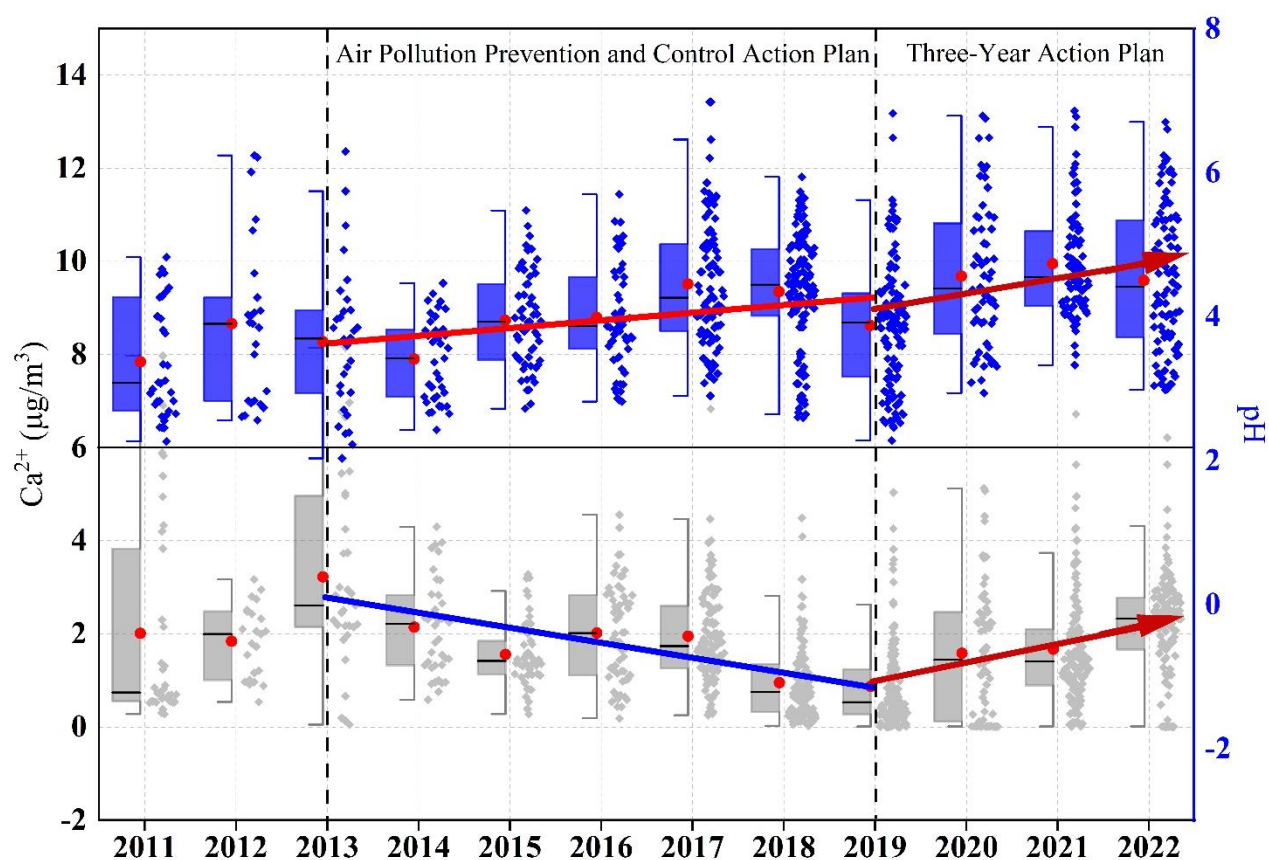
revisions: “Emerging concerns regarding aerosol acidity trends have been highlighted amid China’s sustained initiatives to mitigate emissions of both acidic and alkaline precursors, especially in North China, which is significantly affected by dust aerosol.”

2. Line 19: It should be “12-year”.

Response: Done!

3. Graphical abstract: Please use a different color for the pH. Apparently, the color light blue is too bright for visualization.

Response: Done!



4. Line 57: Please use a word different than “research hotspot”.

Response: OK. We have revised “research hotspot” to “research focus”.

5. Line 64: Please use a different term instead of “fostered a persistent belief”.

Response: This sentence has been deleted referring to Reviewer 1.

6. Eq 4: It should be “ NH_4^+ ”.

Response: Done!

7. Figures in main text and SI: the labels for x- and y- axis and annotations are too small to read.

All figures need to be modified for better visualization.

Response: Done!

8. Lines 173 and 174: more effective than what?

Response: Sorry for the misunderstanding. This sentence has been deleted referring to Reviewer 1.

9. Line 246: NO_3^- can be used to replace nitrate ions.

Response: Done!

10. Line 252: $\text{SO}_4^{2-}/\text{NO}_3^-$ can means the ratio between SO_4^{2-} and NO_3^- . I assume the authors use “/” to represent “or” here. If so, please use the word “or”

Response: Done!

11. The format of “ TNH_x ” should be consistent throughout the manuscript.

Response: Done!

12. Some color choices in figures need to be reconsidered. Certain annotations in color are not color-friendly for visualization.

Response: Thanks for your suggestion. The colors of the figures in both the main text and supplement have been adjusted to enhance their readability.

Manuscript

Measurement report: Crustal materials play an increasing role in elevating particle pH: Insights from 12-year records in a typical inland city of China.

Hongyu Zhang^{1,2}, Shenbo Wang^{2,3*}, Zhangsen Dong^{1,2*}, Xiao Li^{2,3}, Ruiqin Zhang^{2,3}

¹ Collage of Chemistry, Zhengzhou University, Zhengzhou, 450000, China

² Research Institute of Environmental Sciences, Zhengzhou University, Zhengzhou 450000, China

³ School of Ecology and Environment, Zhengzhou University, Zhengzhou, 450000, China

* Corresponding authors: Shenbo Wang and Zhangsen Dong

E-mail address: shbwang@zzu.edu.cn and dzszzu1990@163.com

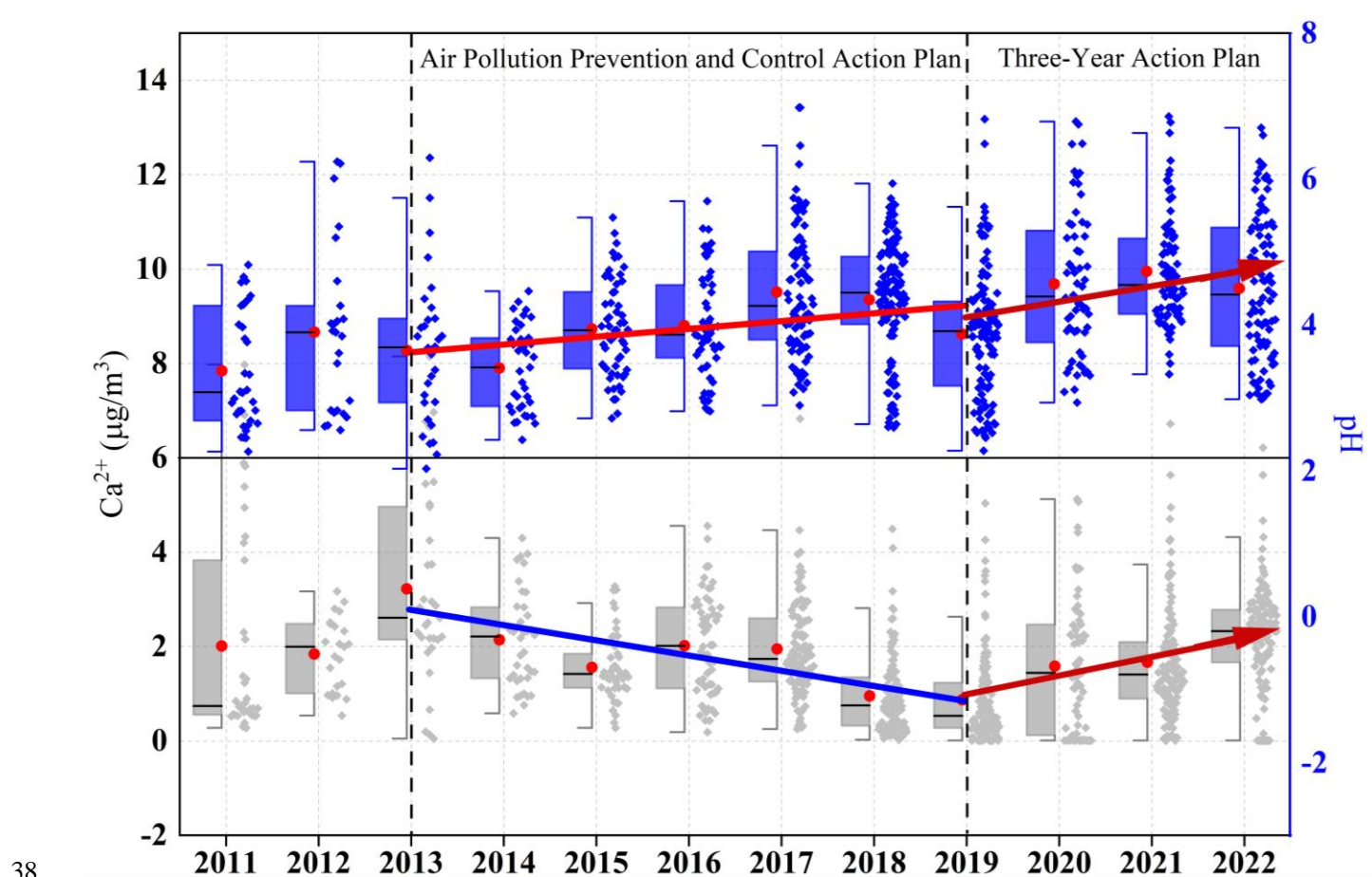
Abstract

Particle acidity serves as a key determinant in atmospheric chemical processes. Emerging concerns regarding aerosol acidity trends have been highlighted amid China's sustained initiatives to mitigate emissions of both acidic and alkaline precursors, especially in North China, which is significantly affected by dust aerosol. 12-year observational data in Zhengzhou reveal that the annual average PM_{2.5} concentration decreased from $162 \pm 81 \mu\text{g}/\text{m}^3$ in 2011 to $60 \pm 41 \mu\text{g}/\text{m}^3$ in 2022, with the largest reduction in sulfate (73%). Correspondingly, the annual particle pH increased by 0.10 units from 2011 to 2019. In addition, the elevated particle pH in 2015 and 2018 was notably influenced by the increase in TNH_x (NH₃ + NH₄⁺). Note that the crustal material concentrations and their proportions increased significantly during 2019–2022, which might be responsible for the resuspension of surrounding soil dust. Even though the TNH_x concentration was decreasing, the annual average growth rate of pH values increased to 0.21 units from 2019 to 2022. This phenomenon is not unique to Zhengzhou, as major cities in the North China Plain have also experienced a pronounced upward trend in coarse particles after 2019. Therefore, the long-term evolution of particle acidity in North China will require comprehensive consideration of synergistic effects involving acidic precursors, ammonia, and crustal materials.

Keywords: Dust, aerosol acidity, sources, North China Plain, control measurement

Synopsis: The future ammonia reduction policies in North China may not lead to a rapid increase in particle acidity in the presence of crustal materials., which further elevated the particle pH after 2019.

37 Graphical abstract:



39 Highlights:

- 40 • Crustal material concentrations and their proportions increased significantly during 2019–2022;
- 41 • The resuspension of surrounding soil dust may determine the rebound of crustal material
- 42 concentrations;
- 43 • Rebound in crustal material further elevated the particle pH.

44 1 Introduction

45 Particle acidity is a critical parameter that affects atmospheric chemistry, such as the gas-particle

partitioning of semi-volatile and volatile species (Surratt et al., 2010; Guo et al., 2016), the solubility of metals (Tao and Murphy, 2019), acid-catalyzed reactions (Rengarajan et al., 2011), and acid deposition (Mao et al., 2009), thereby determining aerosol concentration and chemical composition, as well as impacting human health, ecosystems, and climate (Li et al., 2017; Pye et al., 2020; Su et al., 2020; Nenes et al., 2021). Generally, the global fine particulate matter ($\text{PM}_{2.5}$, aerodynamic diameter $\leq 2.5 \mu\text{m}$) exhibits a bimodal pH distribution ranging from 1–3 (e.g., in the United States and Europe) (Guo et al., 2015; Battaglia et al., 2017; Masiol et al., 2020; Zhang et al., 2021) and 4–5 (e.g., in East Asia) (Kim et al., 2022; Sharma et al., 2022). The atmosphere rich in gaseous ammonia (NH_3) and crustal material (CM) shows significant pH buffering effects (Wang et al., 2020; Zheng et al., 2020; Karydis et al., 2021), which is a dominant factor that drives the high particle pH in East Asia (Karydis et al., 2021; Zhang et al., 2021; Kim et al., 2022; Sharma et al., 2022).

In recent years, the changing trends in particle pH have become a research focus, especially in China, in response to air pollution control policies, i.e. Air Pollution Prevention and Control Action Plan (2013–2018) and Three-Year Action Plan (2018–2020). The annual average $\text{PM}_{2.5}$ concentration in Beijing dropped by 64% from $89.5 \mu\text{g}/\text{m}^3$ in 2013 to $32 \mu\text{g}/\text{m}^3$ in 2023 (MEP, 2023), with a clear downward trend of sulfate concentration, and nitrate surpassing sulfate as the primary component (Zhai et al., 2019; Zhou et al., 2019; Li et al., 2023). The atmospheric behavior of ammonium, governed by gas-particle partitioning processes involving ammonia (NH_3) as the predominant alkaline gas, demonstrates notable stability in concentration levels, with observational records showing less than 5% interannual variation in NH_3 column densities over North China during 2015–2019 (Dong et al., 2023). Under such conditions, the dominant inorganic aerosol component transitions from ammonium sulfate

67 to ammonium nitrate. This compositional shift enhances atmospheric particulate hygroscopicity due
68 to ammonium nitrate's superior water uptake capability, ultimately elevating particle pH levels through
69 aqueous-phase dilution mechanisms (Wexler and Seinfeld, 1991; Pinder et al., 2007, 2008; Heald et
70 al., 2012; Weber et al., 2016). For instance, a significant increase in the nitrate-to-sulfate molar ratio
71 from 2014–2017 in Beijing resulted in the particle pH increasing from 4.4 to 5.4 (Xie et al., 2020).
72 Moreover, increased NH_3 concentrations raised particle pH by 0.3–0.4 units from 2014/2015 to
73 2018/2019 in Beijing (Song et al., 2019). Over Europe and North America, the pH has increased
74 strongly from about 2.8 and 2.2 during the 1970s to 3.9 and 3.3 in 2020 respectively, especially during
75 the 1990s, with significantly increasing NH_3 emission (Karydis et al., 2021). On the contrary, modeling
76 results indicate a continuous decline in pH in East Asia from 1970 to 2020 due to sharp increases in
77 SO_2 and NO_x emissions (Karydis et al., 2021). In addition, the $\text{PM}_{2.5}$ pH showed a slight decrease of
78 0.13 from 2018 to 2022 summer in Beijing due to the change in total nitrate ($\text{NO}_3^- + \text{HNO}_3$) (Li et al.,
79 2023). Moreover, Zhou et al. (2022) found a decreasing pH trend from 2011 to 2019 in eastern China,
80 primarily influenced by temperature, followed by sulfate and non-volatile cations. Similarly, Nah et al.
81 (2023) observed a decreasing pH trend from 2011 to 2020 in Hong Kong, attributing it to temperature
82 and sulfate levels. Thus, concerns have been raised about the potential increase in the acidity of aerosol
83 and precipitation due to China's ongoing efforts to reduce ammonia emissions, which pose severe
84 health risks and acid deposition (Liu et al., 2019; Shi et al., 2019).

85 In addition to NH_3 , CM is another key alkaline substance, that buffers particle pH. Ca^{2+} can form
86 insoluble CaSO_4 with sulfate, reducing sulfate concentration in the aqueous phase of aerosol, and thus
87 lowering H^+ and aerosol liquid water content (ALWC) concentrations and enhancing particle pH (Ding

et al., 2019; Karydis et al., 2021). Moreover, non-volatile cations can lower the molar ratio of ammonia to sulfate, leading to an increase in particle pH (Zheng et al., 2022). Karydis et al. (2021) framework demonstrated that CM played a critical buffering role in sustaining aerosol pH around 7 across the Middle East arid regions. The model sensitivity tests revealed that under hypothetical dust-free conditions (CM = 0), aerosol acidity would escalate to pH~4 due to $\text{NH}_4^+/\text{SO}_4^{2-}$ domination. Wang et al. (2022) reported that non-volatile cations accounted for approximately 8–17% of hourly aerosol pH variation. Li et al. (2023) indicated that the buffering effect of cations was the major reason for the relatively small pH changes from 2018 to 2022 in Beijing, emphasizing that reducing coarse particle emissions in the future could significantly decrease particle pH. In addition, there was a rising trend in the contribution of CM to particle pH in Tianjin, China (Shi et al., 2017). Therefore, it is evident that CM has a significant impact on the variation of particle pH, especially in North China, which is significantly affected by dust aerosol, but the trend of CM concentration and its long-term implication is still lacking unfortunately.

Zhengzhou presents unique atmospheric chemistry that distinguishes it from other mega-cities in North China. As the capital of China's foremost agricultural province (Henan Province, contributing 18% of national NH_3 emissions), Zhengzhou's $\text{PM}_{2.5}$ composition combined substantial crustal material ($15 \pm 3\%$ in $\text{PM}_{2.5}$ vs. $<10\%$ in Beijing) with exceptional ammonia abundance (Huang et al., 2012; Liu et al., 2018; Wang et al., 2018). This created distinct particle acidity characteristics, maintaining pH 4.5–6.0 compared to lower pH levels (3.3–5.4) in other cities like Beijing (Ding et al., 2019; Zhang et al., 2021). However, two critical research gaps persist: (1) the long-term evolution of CM under control policies remains unquantified; (2) the role of CM on pH buffer capacity in NH_3 -

enriched environments lacks systematic assessment.

To address these gaps, our study pioneers the first multi-decadal analysis (2011–2022) coupling PM_{2.5} components with thermodynamic modeling through three key innovations: (1) revealing the long-term trends of CM, (2) analyzing the variations of CM sources, and (3) exploring pH trend and its relationship with CM. The resultant findings advance our understanding of urban aerosol acidity chemistry by underscoring the critical role of CM.

2 Experiment and method

2.1 Instruments and Measurements

Sampling was conducted on the fourth-floor platform at Zhengzhou University (34.75° N, 113.61° E) in Zhengzhou, China. The sampling site (Fig. S1), approximately 14 m above the ground, is primarily surrounded by residential areas with well-developed transportation networks and no significant industrial sources. There are two highways located 3 km to the south and 7 km to the east. Additionally, a coal-fired power plant located 6 km to the east was shut down in 2020, and a gas-fired power plant is situated 3 km to the south.

Samples were collected using a high-volume sampler (TE-6070D, Tisch, USA) and air particulate samplers (TH-16A, Tianhong, China) from April 2011 to December 2022. Two quartz filters and two Teflon filters were used daily from 10:00 AM to 9:00 AM the next day, resulting in a total of 5848 samples. After excluding abnormal data due to instrument malfunctions, 4228 valid samples were obtained. Detailed information on the samples is provided in Table S1. Organic carbon (OC) and elemental carbon (EC) were analyzed using a carbon analyzer (Model 5L, Sunset Laboratory, USA).

Water-soluble inorganic ions (Cl^- , NO_3^- , SO_4^{2-} , Na^+ , NH_4^+ , K^+ , Mg^{2+} , and Ca^{2+}) were measured using ion chromatography (ICS-90 and ICS-900 models, Dionex, USA) (Yu et al., 2017; Jiang et al., 2018). Elements were analyzed using a wavelength dispersive X-ray fluorescence spectrometer (S8 TIGER, Bruker, Germany) to determine concentrations of Fe, Na, Mg, Al, Si, Cl, K, Ca, V, Ni, Cu, Zn, Cr, Mn, Co, Cd, Ga, As, Se, Sr, Sn, Sb, Ba, and Pb (Tremper et al., 2018). Meteorological conditions, including temperature (T), relative humidity (RH), and wind speed (WS) were obtained using an automatic weather station (Wang et al., 2019). Blank filters were also routinely analyzed with each batch of samples to detect sample contamination and provide quality assurance on the elemental concentrations. Detailed analytical methods and quality control are described in the supplement (Text S1). The method detection limits and measurement uncertainties are summarized in Table S2. The quality assurance protocol excluded temporally discrete dust storm and precipitation periods to prevent contamination of the source analysis of CM and modeling particle pH, given that such events induce non-representative extremes in both crustal element concentrations and pH values, coupled with elevated PM measurement uncertainties. The annual mean $\text{PM}_{2.5}$ concentration data for cities in the North China Plain were obtained from the China National Environmental Monitoring Center (CNEMC), available at <https://www.cnemc.cn/>.

2.2 Data Analysis

2.2.1 Mass reconstruction

The calculation method for CM is as follows (Tian et al., 2016):

$$[\text{CM}] = 1.89 \times [\text{Al}] + 2.14 \times [\text{Si}] + 1.4 \times [\text{Ca}] + 1.43 \times [\text{Fe}] + 1.94 [\text{Ti}] \quad (1)$$

where [Al], [Si], [Ca], [Fe] and [Ti] represent the concentrations of the respective elements ($\mu\text{g}/\text{m}^3$), but Ti was not measured.

2.2.2 Thermodynamic model

The particle pH was calculated using the ISORROPIA-II mode (version 2.1, <http://isorrophia.eas.gatech.edu>). The input data (excluding $\text{RH} \leq 30\%$), including SO_4^{2-} , TNO_3 ($\text{HNO}_3 + \text{NO}_3^-$), TNH_x ($\text{NH}_3 + \text{NH}_4^+$), Ca^{2+} , K^+ , Na^+ , Mg^{2+} , Cl^- , RH and T, with the temporal resolution aligned with the sampling periods (from 10:00 AM to 9:00 AM the following day). Input data (excluding $\text{RH} \leq 30\%$) included SO_4^{2-} , TNO_3 ($\text{HNO}_3 + \text{NO}_3^-$), TNH_x ($\text{NH}_3 + \text{NH}_4^+$), Ca^{2+} , K^+ , Na^+ , Mg^{2+} , Cl^- , RH and T. The concentrations of hydrogen ions in air (H_{air}^+) and ALWC were calculated using the aerosol equilibrium composition system $\text{Na}^+ - \text{K}^+ - \text{Ca}^{2+} - \text{Mg}^{2+} - \text{NH}_4^+ - \text{SO}_4^{2-} - \text{NO}_3^- - \text{Cl}^- - \text{H}_2\text{O}$ H_{air}^+ (Fountoukis and Nenes, 2007). pH values were calculated using the following formula:

$$\text{pH} = -\log_{10} \text{H}_{\text{aq}}^+ \cong -\log_{10} \frac{1000 \text{H}_{\text{air}}^+}{\text{ALWC}_i + \text{ALWC}_o} \cong -\log_{10} \frac{1000 \text{H}_{\text{air}}^+}{\text{ALWC}_i} \quad (2)$$

$$\text{ALWC}_o = \frac{m_{\text{org}} \rho_w}{\rho_w} \frac{K_{\text{org}}}{\left(\frac{1}{\text{RH}} - 1 \right)} \quad (3)$$

where ALWC_i and ALWC_o refer to the ALWC for inorganic and organic components, respectively. m_{org} denotes the mass of organic aerosol, ρ_w is the density of water ($1.0 \text{ g}/\text{cm}^3$), ρ_{org} is the density of organic material ($1.4 \text{ g}/\text{cm}^3$) (Guo et al., 2015), K_{org} is the hygroscopicity parameter for organic aerosol (0.087) (Chang et al., 2010; Li et al., 2016). The ISORROPIA-II model operated under metastable conditions in the forward mode. Due to the lack of measured data for gaseous HNO_3 and NH_3 , TNO_3 was represented solely by NO_3^- . The concentration of NH_3 was simulated based on a linear regression

equation proposed by Wei et al. (2023), who used the same data as this study from 2013 to 2020:

$$\text{NH}_3 = 19.909 \times \text{RH} + 0.559 \times \text{T} - 0.35 \times \text{NH}_4^+ + 0.123 \times \text{NO}_3^- + 2.159 \times \text{Cl}^- - 0.224 \times \text{SO}_4^{2-} - 154.923 \quad (4)$$

where NO_3^- , SO_4^{2-} , NH_4^+ , and Cl^- correspond to their respective concentrations ($\mu\text{g}/\text{m}^3$). To validate the applicability of Equation 4 for annual NH_3 estimation and pH simulation in Zhengzhou, this study utilized both observed NH_3 data (from a Thermo Scientific URG-9000D ambient ion monitor, USA) and calculated NH_3 values derived from Equation 4 at the same monitoring site throughout 2022, inputting them into the thermodynamic model for pH simulation. As shown in Figure S2, pH values calculated from observed and simulated NH_3 exhibit good agreement ($r = 0.97$, $P < 0.01$). Furthermore, NH_3 concentrations modeled by ISORROPIA demonstrate a significant correlation ($r = 0.95$, $P < 0.01$) with that simulated NH_3 by Equation 4. These results collectively demonstrate the reliability of the NH_3 estimation method in this study.

2.2.3 HYSPLIT analysis

Backward trajectories were calculated using the mixed-particle Lagrangian integrated trajectory method (HYSPLIT, https://www.ready.noaa.gov/HYSPLIT_traj.php). Meteorological input data were from the Global Data Assimilation System (GDAS) with 3D wind vectors, temperature, relative humidity, geopotential height, surface pressure, and boundary layer diagnostics. 24-h backward trajectories were simulated for air masses above 1000 m above ground level in Zhengzhou. While the surface elevation of Zhengzhou is approximately 100 m above sea level (ASL), setting the height at 1000 m ASL takes into account the minimum altitude needed to traverse the average elevation of the Taihang Mountains (ranging from 1000 to 1500 m ASL). This ensures that the simulated trajectory paths over this topographical barrier are physically realistic.

The Angle Distance algorithm was used to cluster air mass trajectories, enabling the identification of dominant air mass directions and potential pollution sources affecting the study site during different periods. The optimal number of clusters was determined by evaluating the spatial variance (SPVAR) of each trajectory from the cluster mean and the total spatial variance (TSV). The final classification was selected just before the second rapid increase in TSV. The underlying principle is that TSV initially rises sharply during clustering, then increases gradually; however, once the number of clusters reaches a certain threshold, TSV surges again, indicating that the merged clusters are highly dissimilar, marking the end of the classification process. The classification results correspond to the different air mass categories before this final merging step. The mean trajectories of these clusters represent the primary airflow patterns at the target site during the analysis period (Wang et al., 2009). Subsequently, trajectories from two periods, 2013–2018 and 2019–2022, were clustered separately to analyze the variations between the two policy implementation periods.

3 Results and discussion

3.1 Temporal variations in chemical components

Over the past twelve years, the Chinese government implemented the Air Pollution Prevention and Control Action Plans (2013–2018) and the Three-Year Action Plan (2018–2020). The Air Pollution Prevention and Control Action Plan focused on reducing $PM_{2.5}$ concentrations in key regions and aiming to cut $PM_{2.5}$ levels by 10–25% in priority areas over five years. To achieve these goals, it adopted several measures. In terms of industrial restructuring, it mandated the elimination of a large amount of outdated production capacity in industries such as iron/steel and cement to optimize the

209 industrial structure and reduce high-pollution production. For emission standards, it set strict
210 requirements for multiple industrial sectors, especially coal-fired power plants, and gradually
211 introduced ultra-low emission requirements to control pollutants like SO₂, NO_x, and PM. Regarding
212 energy transition, it promoted a shift from coal to cleaner energy sources, including capping coal
213 consumption in certain regions and restricting the construction of small-scale coal-fired boilers.
214 Subsequently, the Three-Year Action Plan was carried out to continue improving air quality with a
215 broader scope of regions under control, further reducing pollutant emissions and enhancing the overall
216 air quality index. The measures included enhanced transportation controls, such as introducing stricter
217 vehicle emission standards (like National VI standards for vehicles) and establishing diesel truck
218 exclusion zones in many cities to reduce emissions from the transportation sector. It also adopted
219 precision governance through grid-based environmental supervision, dividing areas into small grids
220 for more accurate and efficient monitoring of pollution sources. Additionally, it strengthened the legal
221 and institutional framework by revising relevant laws, such as the Air Pollution Prevention and Control
222 Law, to strengthen legal penalties for environmental violations and implementing an environmental
223 tax system to encourage enterprises to reduce emissions.

224 The long-term trends in PM_{2.5} concentrations and its chemical components in Zhengzhou from
225 2011 to 2022 are depicted in Fig. 1, with annual average concentrations listed in Table 1.
226 Correspondingly, the annual average concentration of PM_{2.5} in Zhengzhou decreased from 162 ± 81
227 $\mu\text{g}/\text{m}^3$ in 2011 to $60 \pm 41 \mu\text{g}/\text{m}^3$ in 2022, representing a reduction of approximately 63%. In particular,
228 the reduction rate reached 72% after 2013. As for chemical components, the largest reductions were
229 observed in SO₄²⁻ (79%), decreasing from $38.0 \pm 19.9 \mu\text{g}/\text{m}^3$ in 2013 to $7.9 \pm 4.5 \mu\text{g}/\text{m}^3$ in 2022,

230 followed by EC (76%). Additionally, the concentrations of NH_4^+ and NO_3^- also significantly decreased
231 by 68% and 56%, respectively. The proportion of each component in $\text{PM}_{2.5}$ (Fig. S3) reveals a decrease
232 in SO_4^{2-} , K^+ , and Cl^- , indicating effective control measures targeting coal and biomass combustion
233 (Lei et al., 2021). However, the proportions of NO_3^- and OC in $\text{PM}_{2.5}$ rose from 11% and 12% in 2013
234 to 13% and 17% in 2022, respectively, similar to the trend observed in the North China Plain (Wen et
235 al., 2018; Zhai et al., 2019; Li et al., 2023).

236 3.2 Temporal variations in CM

237 Notably, there is no clear declining trend in the CM concentration, with a rebound observed during
238 2020–2022 (Fig. 1i). Furthermore, the proportion of CM in $\text{PM}_{2.5}$ exhibits a significant upward trend
239 (Fig. S3). To further analyze its trend, sampling data were divided into three periods corresponding to
240 governmental stages: 2011–2013, when no special control measures were implemented; 2013–2019,
241 coinciding with the implementation of the Air Pollution Prevention and Control Action Plan; and
242 2019–2022, coinciding with the Three-Year Action Plan. During these periods, Henan Province and
243 Zhengzhou City implemented several dust control policies summarized in Table S3. As shown in Fig.
244 2a and 2b, the mass concentration of CM peaked at $14.6 \pm 8.3 \mu\text{g}/\text{m}^3$ in 2013, accounting for 8% of
245 $\text{PM}_{2.5}$. To evaluate the inter - annual change trend of CM, the Mann - Kendall method, Sen's slope,
246 and Least - Squares (LS) slope were comprehensively used with the results presented in Table S4.
247 From 2013 to 2019, the CM concentration notably decreased from 14.6 ± 8.3 to $8.5 \pm 7.8 \mu\text{g}/\text{m}^3$, with
248 an annual average decline rate of $0.81 \mu\text{g}/(\text{m}^3 \cdot \text{year})$ from LS slope [$0.015 \mu\text{g}/(\text{m}^3 \cdot \text{year})$ from Sen's
249 slope]. Apart from control measures, the interannual meteorological analysis shows (Fig. S4) WS
250 exhibited a declining trend, with a decrease rate of 43%, while RH showed an increasing trend at a rate

251 of 8% from 2013 to 2019, under which conditions that were unfavorable for dust resuspension (Wang
 252 et al., 2013, 2018). Seasonal trends (Fig. S5) reveal significant declines in CM during spring in 2013–
 253 2019 with WS decreasing from 2.2 m/s in 2013 to 1.4 m/s in 2019 (Fig. S6) and stable RH (Fig. S7).
 254 Similarly, summer CM reductions in 2013–2019 corresponded with WS declines. These patterns
 255 suggest spring-summer CM improvements resulted from the synergistic effects of meteorological
 256 changes and dust control policies. Conversely, autumn-winter seasons showed limited CM reductions
 257 despite comparable WS decreases in 2013–2019, highlighting the need for enhanced dust emission
 258 controls in Zhengzhou during these seasons. As for the individual crustal elements in Fig. S8, Ca
 259 exhibited the highest average annual decline rate of 33% during 2013–2019, followed by Al. Si showed
 260 a less pronounced decline, attributed to its association with soil dust, where control measures for
 261 exposed soil are lacking (Zhang et al., 2020). In addition, the Ca^{2+} concentration as depicted in Fig. 2c
 262 decreased from $3.2 \pm 2.1 \mu\text{g}/\text{m}^3$ in 2013 to $2.2 \pm 1.1 \mu\text{g}/\text{m}^3$ in 2019, with an approximate annual average
 263 decline rate of $0.32 \mu\text{g}/(\text{m}^3 \cdot \text{year})$ from LS slope [$4.14\text{E}-03 \mu\text{g}/(\text{m}^3 \cdot \text{year})$ from Sen's slope] in Table S4,
 264 further demonstrating the decline in dust source. It was worth noting that the proportions of CM, Ca,
 265 Al, Fe, Si, and Ca^{2+} in $\text{PM}_{2.5}$ have shown consecutive annual increases from 2013 to 2019, with CM
 266 proportion increasing from 8% in 2013 to 14% in 2019, indicating that CM reduction lagged behind
 267 $\text{PM}_{2.5}$ reduction efforts in Zhengzhou during this period. Additionally, both concentration and
 268 proportion of Ca^{2+} in 2022 ($2.2 \pm 1.1 \mu\text{g}/\text{m}^3$ and 14%) were higher than in other cities of China, such
 269 as Beijing ($1.0 \mu\text{g}/\text{m}^3$ and 2.8%), Tianjin ($0.5 \mu\text{g}/\text{m}^3$ and 1.4%), and Xiamen ($0.48 \mu\text{g}/\text{m}^3$ and 1.5%)
 270 (Shi et al., 2017; Xu et al., 2025; Zhang et al., 2021). These results indicate that CM remained an
 271 important component of $\text{PM}_{2.5}$ in Zhengzhou City.

During 2019–2022, both CM and Ca^{2+} concentrations exhibited significant rebounds, with annual growth rates of 0.24 and 0.4 $\mu\text{g}/(\text{m}^3 \cdot \text{year})$ from LS slope [5.80E–03 and 5.42E–03 $\mu\text{g}/(\text{m}^3 \cdot \text{year})$ from Sen's slope], respectively, and their proportions increased from 14% and 2% in 2019 to 22% and 5% in 2022. CM concentrations rebounded in all seasons, particularly in winter (Fig. S5). Changes in meteorological conditions may be a significant factor contributing to these concentration rebounds, accompanied by the average WS increased by 0.14 m/s and RH decreased by 7% from 2020 to 2022 (Fig. S4, S6, and S7), facilitating dust resuspension. Furthermore, the lack of more effective dust control measures, as indicated by the absence of significant changes in the dust control policies from the Air Pollution Prevention and Control Action Plan and Three-Year Action Plan, may be another important factor contributing to the rebound of dust.

3.3 Sources of CM

Elemental ratios were employed to characterize the sources of CM, with the Ca/Al ratio widely recognized as a reliable indicator of sandy origin (Zhang et al., 2017). In addition, significant variations in Ca/Si ratios (Table S5) were observed among different dust sources (Road, Construction, Piles, Soil). Fig. 3a illustrates the trend in Ca/Si ratios from 2011 to 2022. After 2013, Ca/Si ratios showed a declining trend annually, with the average ratio decreasing from a peak of 1.6 in 2016 to a lowest of 0.4 in 2022. Compared with Ca/Si ratios from different types of dust sources, the effect of road and construction dust on CM has gradually decreased. This may be attributed to the implementation of dust control measures such as enclosure, shielding, and dust suppression at construction and demolition sites, as well as dust control on ground surfaces and roads (Table S5). During 2019–2022, the average Ca/Si ratio remained below 1, with a mean of 0.4 in 2022, indicating that soil dust predominantly

contributed to CM. Currently, measures for controlling soil-suspended dust are limited, primarily relying on long-term strategies such as afforestation and increasing urban green coverage, thus requiring a longer process and sustained investment.

Sand dust transport serves as a significant source of CM in the North China Plain (Zhang et al., 2024). The Ca/Al ratio from 2016 to 2022 (Fig. 3b) shows minimal variation, with annual averages ranging between 1.5 and 2.5, indicating no significant changes in the source regions of sand. The transport trajectories reveal that the predominant pathways for long-distance transport of sand dust originated from Inner Mongolia, passing through Shaanxi and Shanxi provinces. Compared to 2013–2018 (45%), the influence of long-distance transport decreased to 25% during 2019–2022. In contrast, local transport within Henan province and short-distance transport from Shandong province showed a noticeable increase. These findings suggest that the rebound in CM concentrations during 2019–2022 in Zhengzhou might be responsible for the resuspension of surrounding soil dust.

3.4 Long-term trend of particle pH

Are shown in Fig. 4 and Table S4, pH values showed a clearly increasing trend after 2014. From 2013 to 2019, the annual pH increased by 0.11 units from the LS slope [$9.15\text{E}-04$ units from Sen's slope], reaching a maximum median value of 4.45 (Mean: 4.35) in 2018. Note that the annual average growth rate of pH values increased to 0.21 units from LS slope [$2.93\text{E}-03$ units from Sen's slope] from 2019 to 2022, with a maximum median value of 4.42 (Mean: 4.51) in 2022. Seasonally, pH values showed increasing trends in spring, summer, and autumn, and notably increased in winter from 2020 to 2022 (Fig. S9). The increasing trend in pH values observed in this study is similar to the findings in Beijing (Song et al., 2019; Xie et al., 2020), presumably attributable to the comparable chemical

314 composition trends and meteorological conditions. In contrast, Shanghai and Hong Kong display
315 divergent trends (Nah et al., 2023; Zhou et al., 2022). This disparity might be ascribed to the stronger
316 buffering effect exerted by NH_3 and dust in Zhengzhou than marine aerosols (Na^+/Cl^-) in these coastal
317 cities (Shi et al., 2017; Liu et al., 2019). Moreover, the relatively higher temperatures and more
318 abundant rainfall in Shanghai and Hong Kong could also contribute to the distinct trends observed in
319 their pH values.

320 Sensitivity analyses were conducted to explore the dominant factors driving the elevated particle
321 pH in Zhengzhou by giving a range for one parameter (i.e., TNH_x) and average values for other
322 parameters (i.e., SO_4^{2-} , NO_3^- , Na^+ , Cl^- , Ca^{2+} , K^+ , Mg^{2+} , RH, and T) input into the ISORROPIA-II model.

323 Are shown in Fig. S10, particle pH increases with the cation concentrations (e.g., TNH_x , K^+ , Ca^{2+} ,
324 Mg^{2+} , and Na^+) and decreases with anions concentrations (e.g., SO_4^{2-} and NO_3^-). Additionally, RH
325 does not significantly affect pH, whereas an increase in T leads to a noticeable decrease in particle pH.

326 Based on the sensitivity analysis curves, the pH values corresponding to a variable in different
327 years were calculated according to the average values of this variable in different years (Table S6). The
328 difference in pH values of this variable between two adjacent years was defined as ΔpH which is
329 illustrated in Fig. 5. According to Equation (2), in addition to H^+ concentration, particle pH is primarily
330 influenced by the dilution effect of ALWC. Moreover, ALWC affects the gas-particle partitioning of
331 semi-volatile compounds, thereby influencing particle acidity (Zuend et al., 2010; Zuend and Seinfeld,
332 2012). As shown in Fig.5 and Table S6, only in 2015, 2019, and 2020 did the increases in ALWC
333 concentration ($17.6 \mu\text{g}/\text{m}^3$, $4.1 \mu\text{g}/\text{m}^3$, and $11.6 \mu\text{g}/\text{m}^3$, respectively) lead to pH increases of 0.22, 0.06,
334 and 0.14 units. This clearly cannot fully explain the significant pH increase in Zhengzhou since 2013.

335 Notably, since 2013, H^+ concentration has shown a decreasing trend. Particularly, H^+ concentrations
336 decreased by 7.6×10^{-6} , 11.2×10^{-6} , and 7.2×10^{-6} mol/L in 2013, 2015, and 2017, respectively,
337 leading to pH increases of 0.21, 0.36, and 0.42 units. After 2019, a continuous decline in H^+
338 concentration was observed for three consecutive years, resulting in pH increases of 0.21, 0.13, and
339 0.2 units in 2020, 2021, and 2022, respectively. These findings indicate that the increase in pH from
340 2019 to 2022 in Zhengzhou was primarily driven by the reduction in H^+ concentration.

341 The concentration of H^+ in the aerosol liquid phase is influenced by both chemical composition
342 and meteorological conditions. To further understand the factors affecting ΔpH , we analyzed the
343 variations in $PM_{2.5}$ chemical components and meteorological parameters. Results indicate that the
344 decline in SO_4^{2-} from 2013 to 2018 was the primary cause of the increase in particle pH, as it decreased
345 H^+ and ALWC concentrations (Fig. S11) in aerosol (Ding et al., 2019; Zhang et al., 2021). The average
346 SO_4^{2-} concentration decreased by 14.6 and 5.3 $\mu g/m^3$, resulting in a pH increase of 0.43 and 0.35 units
347 from 2013 to 2014 and 2016 to 2017, respectively, which was comparable to an increased rate of 0.3
348 units in East Asia due to SO_2 emission controls since 2016 (Karydis et al., 2021). As another acidic
349 ion, the decrease in nitrate concentration did not significantly contribute to the pH increases, consistent
350 with findings from Ding et al. (2019) and Zhang et al. (2021). This is primarily because NO_3^- declined
351 more slowly compared to sulfate ions and exceeded sulfate concentrations after 2016, under which
352 conditions that nitrate-rich particles can absorb twice the amount of water that sulfate-rich particles,
353 leading to an increase in ALWC concentration and inhibiting pH decline (Lin et al., 2020; Xie et al.,
354 2020). On the other hand, increases in particle pH in 2015 and 2018 were notably influenced by
355 changes in TNH_x with concentrations increased by 5.5 and 1.3 $\mu g/m^3$, respectively. Increased TNH_x

356 concentrations could react with SO_4^{2-} or NO_3^- and consume a substantial amount of H^+ , thereby raising
357 particulate matter pH values (Seinfeld et al., 1998; Zhang et al., 2021). Substantial decreases in T in
358 2015 (4.2°C), 2017 (4.9°C), and 2018 (2.8°C), favoring NH_3 partitioning into the particle phase and
359 reducing H^+ concentrations, drove increases in particle pH (Tao and Murphy, 2019).

360 During the period from 2020 to 2022, the influence of SO_4^{2-} on particle pH gradually decreased,
361 with a decrease in concentration from 0.3 to 2.3 $\mu\text{g}/\text{m}^3$ (Table S6) only bringing about a pH decrease
362 of 0.03 to 0.14 (Fig. 5). Moreover, a rebound in SO_4^{2-} concentration to $7.9 \pm 4.5 \mu\text{g}/\text{m}^3$ in 2022 even
363 resulted in a decrease of 0.11 units in pH instead. On the other hand, TNHx began to show a slight
364 annual decline (0.9 to 2.2 $\mu\text{g}/\text{m}^3$), resulting in a significant decrease in pH (0.21–0.35). Consequently,
365 the increase in pH values was closely related to the rise in Ca^{2+} concentration. Ca^{2+} is less volatile and
366 competes preferentially with NH_3 to neutralize anions such as SO_4^{2-} to form insoluble CaSO_4 , which
367 precipitates from the aerosol aqueous phase (Ding et al., 2019; Karydis et al., 2021), thereby reducing
368 H^+ concentrations (Fig. S11) and subsequently lowering particle acidity. Specifically, increases of 0.7
369 and 0.5 $\mu\text{g}/\text{m}^3$ in Ca^{2+} concentrations led to pH increases of 0.13 and 0.09 units in 2020 and 2022,
370 respectively, making Ca^{2+} a primary controlling factor for pH elevation.

371 4 Conclusions

372 The annual average $\text{PM}_{2.5}$ concentration in Zhengzhou decreased from $212.4 \pm 101.5 \mu\text{g}/\text{m}^3$ in
373 2013 to $59.5 \pm 41.2 \mu\text{g}/\text{m}^3$ in 2022, with the largest reduction in SO_4^{2-} . As for CM, their concentrations
374 notably decreased from 2013 to 2019, because of effective dust control measures, as well as decreased
375 wind speed and increased relative humidity. However, the proportions of CM in $\text{PM}_{2.5}$ have shown

consecutive annual increases. In addition, CM concentrations and their proportions increased significantly during 2019–2022, which might be responsible for the resuspension of surrounding soil dust. Correspondingly, the annual pH increased by 0.11 units from 2013 to 2019 mainly due to the decline in SO_4^{2-} , increased TNH_x , or decreased temperature. During the period from 2020 to 2022, the annual average growth rate of pH values increased to 0.21 units from 2019 to 2022, which was determined by the rise in Ca^{2+} concentration.

5 Implication

Control measures implemented by the Chinese government have proven effective in reducing dust, but this study reveals that the crustal materials in $\text{PM}_{2.5}$ rebounded after 2019. This phenomenon is not unique to Zhengzhou, as major cities in the North China Plain have also experienced a pronounced upward trend in coarse particles after 2019 (Fig. S12). Thus, crustal materials persist as a substantial constituent of atmospheric aerosols in North China, sustaining elevated particle pH levels. Extensive research has established that heightened particle pH inhibits nitrate reduction in aerosols (Ding et al., 2019; Lin et al., 2020; Wen et al., 2018), particularly significant given nitrate's predominant role in haze formation within this region. Notably, while moderately acidic aerosols demonstrate reduced health impacts, particles with $\text{pH} < 3$ exhibit substantially greater health risks (Shi et al., 2019). Consequently, future environmental management strategies must prioritize real-time assessment of regulatory impacts on particle acidity. This necessitates an integrated approach that simultaneously addresses acidic precursors, alkaline precursors, and crustal material contributions to atmospheric acid chemistry.

396 **Data availability**

397 All the data presented in this article can be accessed through
398 <https://doi.org/10.5281/zenodo.14032007> (Zhang, 2024).

399 **Supporting Information**

400 Additional data, figures, and tables, some of which are referenced directly within the manuscript,
401 and detailed descriptions of field measurements and samples.

402 **Author contributions**

403 Shenbo Wang designed this study. Hongyu Zhang and Zhangsen Dong analyzed the data and
404 prepared the manuscript with the contributions of all coauthors. Xiao Li conducted measurements.
405 Ruiqin Zhang provided funding acquisition. All authors have read and agreed to the published version
406 of the manuscript.

407 **Competing interests**

408 The authors declare that they have no conflict of interest.

409 **Acknowledgment**

410 This work was supported by the National Key Research and Development Program of China (No.

2024YFC3713701), the China Postdoctoral Science Foundation (2023 M733220), the Zhengzhou PM_{2.5} and O₃ Collaborative Control and Monitoring Project (20220347 A), and the National Key R&D Program of China No. 2017YFC0212400.

Funding Sources

This work was supported by the National Key Research and Development Program of China (No. 2024YFC3713701), the China Postdoctoral Science Foundation (2023 M733220), the Zhengzhou PM_{2.5} and O₃ Collaborative Control and Monitoring Project (20220347 A), and the National Key Research and Development Program of China (No. 2017YFC0212400).

References

- Battaglia, M. A.; Douglas, S.; Hennigan, C.: Effect of the urban heat island on aerosol pH, Environ. Sci. Technol., 51, 13095–13103, <https://doi.org/10.1021/acs.est.7b02786>, 2017.
- Chang, R. Y. W.; Slowik, J. G.; Shantz, N. C.; Vlasenko, A.; Liggi, J.; Sjostedt, S. J.; Leaitch, W. R.; Abbatt, J. P. D. The hygroscopicity parameter (κ) of ambient organic aerosol at a field site subject to biogenic and anthropogenic influences: relationship to degree of aerosol oxidation. Atmos. Chem. Phys., 10, 5047–5064, <https://doi.org/10.5194/acp-10-5047-2010>, 2010.
- Ding, J., Zhao, P., Su, J., Dong, Q., Du, X., and Zhang, Y.: Aerosol pH and its driving factors in Beijing, Atmos. Chem. Phys., 19, 7939–7954, <https://doi.org/10.5194/acp-19-7939-2019>, 2019.
- Dong, J., Li, B., Li, Y., Zhou, R., Gan, C., Zhao, Y., Liu, R., Yang, Y., Wang, T., and Liao, H.: Atmospheric ammonia in China: Long-term spatiotemporal variation, urban-rural gradient, and influencing factors, Sci. Total Environ., 883, 163733, <https://doi.org/10.1016/j.scitotenv.2023.163733>, 2023.
- Fountoukis, C and Nenes, A.: ISORROPIA II: a computationally efficient thermodynamic equilibrium

433 model for K^+ - Ca^{2+} - Mg^{2+} - NH_4^+ - Na^+ - SO_4^{2-} - NO_3^- - Cl^- - H_2O aerosols, *Atmos. Chem. Phys.*,
434 7, 4639–4659, <https://doi.org/10.5194/acp-7-4639-2007>, 2007.

435 Guo, H., Sullivan, A. P., Campuzano-Jost, P., Schroder, J. C., Lopez-Hilfiker, F. D., Dibb, J. E., Jimenez,
436 J. L., Thornton, J. A., Brown, S. S., Nenes, A., and Weber, R. J.: Fine particle pH and the
437 partitioning of nitric acid during winter in the northeastern United States, *J. Geophys. Res. Atmos.*,
438 121, 3103–3116, <https://doi.org/10.1002/2016JD025311>, 2016.

439 Guo, H., Xu, L., Bougiatioti, A., Cerully, K. M., Capps, S. L., Hite Jr, J. R., Carlton, A. G., Lee, S. H.,
440 Bergin, M. H., Ng, N. L., Nenes, A., and Weber, R. J.: Fine-particle water and pH in the
441 southeastern United States, *Atmos. Chem. Phys.*, 15, 5211–5228, [https://doi.org/10.5194/acp-15-](https://doi.org/10.5194/acp-15-5211-2015)
442 [5211-2015](https://doi.org/10.5194/acp-15-5211-2015), 2015.

443 Heald, C.; Collett, J. J.; Lee, T.; Benedict, K.; Schwandner, F.; Li, Y.; Clarisse, L.; Hurtmans, D. R.;
444 Van, D. M.; Clerbaux, C.; Coheur, P. F.; Philip, S.; Martin, R. V.; Pye, T.: Atmospheric ammonia
445 and particulate inorganic nitrogen over the United States, *Atmos. Chem. Phys.*, 12, 10295–10312,
446 <https://doi.org/10.5194/acp-12-10295-2012>, 2012.

447 Huang, X., Song, Y., Li, M., Li, J., Huo, Q., Cai, X., Zhu, T., Hu, M., and Zhang, H.: A high-resolution
448 ammonia emission inventory in China, *Global. Biogeochem. Cy.*, 26, GB1030,
449 <https://doi.org/10.1029/2011GB004161>, 2012.

450 Jiang, N.; Duan, S.; Yu, X.; Zhang, R.; Wang, K. Comparative major components and health risks of
451 toxic elements and polycyclic aromatic hydrocarbons of $PM_{2.5}$ in winter and summer in
452 Zhengzhou: Based on three-year data. *Atmos. Res.*, 213, 173–184,
453 <https://doi.org/10.1016/j.atmosres.2018.06.008>, 2018.

454 Karydis, V. A., Tsimpidi, A. P., Pozzer, A., and Lelieveld, J.: How alkaline compounds control
455 atmospheric aerosol particle acidity, *Atmos. Chem. Phys.*, 21, 14983–15001,
456 <https://doi.org/10.5194/acp-21-14983-2021>, 2021.

457 Kim, Y., Park, O., Park, S. H., Kim, M. J., Kim, J.-J., Choi, J.-Y., Lee, D., Cho, S., and Shim, S.: $PM_{2.5}$
458 pH estimation in Seoul during the KORUS-AQ campaign using different thermodynamic models,
459 *Atmos. Environ.*, 268, 118787, <https://doi.org/10.1016/j.atmosenv.2021.118787>, 2022.

460 Lei, L., Zhou, W., Chen, C., He, Y., Li, Z., Sun, J., Tang, X., Fu, P., Wang, Z., and Sun, Y.: Long-term

461 characterization of aerosol chemistry in cold season from 2013 to 2020 in Beijing, China, *Environ.*
 462 *Pollut.*, 268, 115952, <https://doi.org/10.1016/j.envpol.2020.115952>, 2021.

463 Li, C.; Hu, Y.; Chen, J.; Ma, Z.; Ye, X.; Yang, X.; Wang, L.; Wang, X.; Mellouki, A. Physiochemical
 464 properties of carbonaceous aerosol from agricultural residue burning: Density, volatility, and
 465 hygroscopicity. *Atmos. Environ.*, 140, 94–105, <https://doi.org/10.1016/j.atmosenv.2016.05.052>,
 466 2016.

467 Li, W., Xu, L., Liu, X., Zhang, J., Lin, Y., Yao, X., Gao, H., Zhang, D., Chen, J., Wang, W., Harrison,
 468 R. M., Zhang, X., Shao, L., Fu, P., Nenes, A., and Shi, Z.: Air pollution-aerosol interactions
 469 produce more bioavailable iron for ocean ecosystems, *Sci. Adv.*, 3, e1601749,
 470 <https://doi.org/10.1126/sciadv.1601749>, 2017.

471 Li, Y., Lei, L., Sun, J., Gao, Y., Wang, P., Wang, S., Zhang, Z., Du, A., Li, Z., Wang, Z., Kim, J. Y.,
 472 Kim, H., Zhang, H., and Sun, Y.: Significant reductions in secondary aerosols after the Three-
 473 Year Action Plan in Beijing summer, *Environ. Sci. Technol.*, 57, 15945–15955,
 474 <https://doi.org/10.1021/acs.est.3c02417>, 2023.

475 Lin, Y., Zhang, Y., Fan, M., and Bao, M.: Heterogeneous formation of particulate nitrate under
 476 ammonium-rich regimes during the high-PM_{2.5} events in Nanjing, China, *Atmos. Chem. Phys.*,
 477 20, 3999–4011, <https://doi.org/10.5194/acp-20-3999-2020>, 2020.

478 Liu, M.; Huang, X.; Song, Y.; Tang, J.; Cao, J.; Zhang, X.; Zhang, Q.; Wang, S.; Xu, T.; Kang, L.; Gai,
 479 X.; Zhang, H.; Yang, F.; Wang, H.; Yu, J.; Lau, A.; He, L.; Huang, X.; Duan, L.; Ding, A.; Xue,
 480 L.; Gao, J.; Liu, B.; Zhu, T. Ammonia emission control in China would mitigate haze pollution
 481 and nitrogen deposition, but worsen acid rain. *Proc. Natl. Acad. Sci.*, 116, 7760–7765,
 482 <https://doi.org/10.1073/pnas.1814880116>, 2019.

483 Liu, Z., Gao, W., Yu, Y., Hu, B., Xin, J., Sun, Y., Wang, L., Wang, G., Bi, X., Zhang, G., Xu, H., Cong,
 484 Z., He, J., Xu, J., and Wang, Y.: Characteristics of PM_{2.5} mass concentrations and chemical species
 485 in urban and background areas of China: emerging results from the CARE-China network, *Atmos.*
 486 *Chem. Phys.*, 18, 8849–8871, <https://doi.org/10.5194/acp-18-8849-2018>, 2018.

487 Mao, I., Lin, C., Lin, C., Chen, Y., Sung, F., and Chen, M.: Exposure of acid aerosol for
 488 schoolchildren in metropolitan Taipei, *Atmos. Environ.*, 43, 5622–5629, <https://doi.org/10.>

489 [1016/j.atmosenv.2009.07.054](https://doi.org/10.1016/j.atmosenv.2009.07.054), 2009.

490 Masiol, M., Squizzato, S., Formenton, G., Khan, M. B., Hopke, P. K., Nenes, A., Pandis, S. N., Tositti,
 491 L., Benetello, F., Visin, F., and Pavoni, B.: Hybrid multiple-site mass closure and source
 492 apportionment of PM_{2.5} and aerosol acidity at major cities in the Po Valley, *Sci. Total Environ.*,
 493 704, 135287, <https://doi.org/10.1016/j.scitotenv.2019.135287>, 2020.

494 MEP (Ministry of Environment Protection), 2023. [https://www.mee.gov.cn/ywdt/hjywnews/2024](https://www.mee.gov.cn/ywdt/hjywnews/202406/t20240605_1075031.shtml)
 495 [06/t20240605_1075031.shtml](https://www.mee.gov.cn/ywdt/hjywnews/202406/t20240605_1075031.shtml), Accessed date:5 June 2024.

496 Nah, T., Lam, Y. H., Yang, J., and Yang, L.: Long-term trends and sensitivities of PM_{2.5} pH and aerosol
 497 liquid water to chemical composition changes and meteorological parameters in Hong Kong,
 498 South China: Insights from 10-year records from three urban sites, *Atmos. Environ.*, 302,
 499 <https://doi.org/10.1016/j.atmosenv.2023.119725>, 2023.

500 Nenes, A., Pandis, S. N., Kanakidou, M., Russell, A. G., Song, S., Vasilakos, P., and Weber, R. J.:
 501 Aerosol acidity and liquid water content regulate the dry deposition of inorganic reactive nitrogen,
 502 *Atmos. Chem. Phys.*, 21, 6023–6033, <https://doi.org/10.5194/acp-21-6023-2021>, 2021.

503 Pinder, R., Adams, P., and Pandis, S.: Ammonia emission controls as a cost-effective strategy for
 504 reducing atmospheric particulate matter in the eastern United States, *Environ. Sci. Technol.*, 41,
 505 380–386, <https://doi.org/10.1021/es060379a>, 2007.

506 Pinder, R., Gilliland, A., and Dennis, R.: Environmental impact of atmospheric NH₃ emissions under
 507 present and future conditions in the eastern United States, *Geophys. Res. Lett.*, 35, 28,
 508 <https://doi.org/10.1029/2008gl033732>, 2008.

509 Pye, H. O. T.; Nenes, A.; Alexander, B.; Ault, A. P.; Barth, M. C.; Clegg, S. L.; Collett Jr, J. L.; Fahey,
 510 K. M.; Hennigan, C. J.; Herrmann, H.; Kanakidou, m.; Kelly, J. T.; Ku, L.; McNeill, V. F.; Riemer,
 511 N.; Schaefer, T.; Shi, G.; Tilgner, A.; Walker, J.T.; Wang, T.; Weber, R.; Xing, J.; Zaveri, R. A.;
 512 Zuend, A. The acidity of atmospheric particles and clouds. *Atmos. Chem. Phys.*, 20, 4809–4888,
 513 <https://doi.org/10.5194/acp-20-4809-2020>, 2020.

514 Rengarajan, R., Sudheer, A. K., and Sarin, M. M.: Aerosol acidity and secondary organic aerosol
 515 formation during wintertime over urban environment in western India, *Atmos. Environ.*, 45,
 516 1940–1945, <https://doi.org/10.1016/j.atmosenv.2011.01.026>, 2011.

Seinfeld, J. H., Pandis, S. N., and Noone, K. J.: Atmospheric chemistry and physics: From air pollution to climate change, *Phys. Today.*, 51, 88–90, <https://doi.org/10.1063/1.882420>, 1998.

Sharma, B., Jia, S., Polana, A. J., Ahmed, M. S., Haque, R. R., Singh, S., Mao, J., and Sarkar, S.: Seasonal variations in aerosol acidity and its driving factors in the eastern Indo-Gangetic Plain: A quantitative analysis, *Chemosphere.*, 305, 135490, <https://doi.org/10.1016/j.chemosphere.2022.135490>, 2022.

Shi, G., Xu, J., Peng, X., Xiao, Z., Chen, K., Tian, Y., Guan, X., Feng, Y., Yu, H., Nenes, A., and Russell, A. G.: pH of aerosols in a polluted atmosphere: source contributions to highly acidic aerosol, *Environ. Sci. Technol.*, 51, 4289–4296, <https://doi.org/10.1021/acs.est.6b05736>, 2017.

Shi, X., Nenes, A., Xiao, Z., Song, S., Yu, H., Shi, G., Zhao, Q., Chen, K., Feng, Y., and Russell, A. G.: High-resolution data sets unravel the effects of sources and meteorological conditions on nitrate and its gas-particle partitioning, *Environ. Sci. Technol.*, 53, 3048–3057, <https://doi.org/10.1021/acs.est.8b06524>, 2019.

Song, S., Nenes, A., Gao, M., Zhang, Y., Liu, P., Shao, J., Ye, D., Xu, W., Lei, L., Sun, Y., Liu, B., Wang, S., and McElroy, M. B.: Thermodynamic modeling suggests declines in water uptake and acidity of inorganic aerosols in Beijing winter haze events during 2014/2015–2018/2019, *Environ. Sci. Technol. Lett.*, 6, 752–760, <https://doi.org/10.1021/acs.estlett.9b00621>, 2019.

Su, H., Cheng, Y., and Pöschl, U.: New Multiphase Chemical Processes Influencing Atmospheric Aerosols, Air Quality, and Climate in the Anthropocene, *Acc. Chem. Res.*, 53, 2034–2043, <https://doi.org/10.1021/acs.accounts.0c00246>, 2020.

Surratt, J. D., Chan, A. W. H., Eddingsaas, N. C., Chan, M., Loza, C. L., Kwan, A. J., Hersey, S. P., Flagan, R. C., Wennberg, P. O., and Seinfeld, J. H.: Reactive intermediates revealed in secondary organic aerosol formation from isoprene, *Proc. Natl. Acad. Sci.*, 107, 6640–6645, <https://doi.org/10.1073/pnas.0911114107>, 2010.

Tao, Y. and Murphy, J. G.: The sensitivity of PM_{2.5} acidity to meteorological parameters and chemical composition changes: 10-year records from six Canadian monitoring sites, *Atmos. Chem. Phys.*, 19, 9309–9320, <https://doi.org/10.5194/acp-19-9309-2019>, 2019.

Tian, Y.; Chen, G.; Wang, H.; Huang-Fu, Y.; Shi, G.; Han, B.; and Feng, Y.: Source regional

545 contributions to PM_{2.5} in a megacity in China using an advanced source regional apportionment
 546 method. *Chemosphere.*, 147, 256–263, <https://doi.org/10.1016/j.chemosphere.2015.12.132>, 2016.

547 Tremper, A.; Font, A.; Priestman, M.; Hamad, S.; Chung, T.; Pribadi, A.; Brown, R.; Goddard, S.;
 548 Grassineau, N.; Petterson, K.; Kelly, F.; Green, D.: Field and laboratory evaluation of a high time
 549 resolution x-ray fluorescence instrument for determining the elemental composition of ambient
 550 aerosols, *Atmos. Meas. Tech.*, 11, 3541–3557, <https://doi.org/10.5194/amt-11-3541-2018>, 2018.

551 Wang, C., Yin, S., Bai, L., Zhang, X., Gu, X., Zhang, H., Lu, Q., and Zhang, R.: High-resolution
 552 ammonia emission inventories with comprehensive analysis and evaluation in Henan, China,
 553 2006–2016, *Atmos. Environ.*, 193, 11–23, <https://doi.org/10.1016/j.atmosenv.2018.08.063>, 2018.

554 Wang, G., Chen, J., Xu, J., Yun, L., Zhang, M., Li, H., Qin, X., Deng, C., Zheng, H., Gui, H., Liu, J.,
 555 and Huang, K.: Atmospheric processing at the Sea-Land interface over the South China Sea:
 556 Secondary aerosol formation, aerosol acidity, and role of sea salts, *J. Geophys. Res. Atmos.*,
 557 127, <https://doi.org/10.1029/2021jd036255>, 2022.

558 Wang, L., Du, H., Chen, J., Zhang, M., Huang, X., Tan, H., Kong, L., and Geng, F.: Consecutive
 559 transport of anthropogenic air masses and dust storm plume: Two case events at Shanghai, China,
 560 *Atmos. Res.*, 127, 22–33, <https://doi.org/10.1016/j.atmosres.2013.02.011>, 2013.

561 Wang, S., Yin, S., Zhang, R., Yang, L., Zhao, Q., Zhang, L., Yan, Q., Jiang, N., and Tang, X.: Insight
 562 into the formation of secondary inorganic aerosol based on high-time-resolution data during haze
 563 episodes and snowfall periods in Zhengzhou, China, *Sci. Total Environ.*, 660, 47–56,
 564 <https://doi.org/10.1016/j.scitotenv.2018.12.465>, 2019.

565 Wang, S.; Wang, L.; Li, Y.; Wang, C.; Wang, W.; Yin, S.; Zhang, R.; Effect of ammonia on fine-particle
 566 pH in agricultural regions of China: comparison between urban and rural sites, *Atmos. Chem.*
 567 *Phys.*, 20, 2719–2734, <https://doi.org/10.5194/acp-20-2719-2020>, 2020.

568 Wang, Y., Zhang, X., and Draxler, R.: TrajStat: GIS-based software that uses various trajectory
 569 statistical analysis methods to identify potential sources from long-term air pollution
 570 measurement data, *Environ. Model. Softw.*, 24, 938–939,
 571 <https://doi.org/10.1016/j.envsoft.2009.01.004>, 2009.

572 Wang, Z., Pan, X., Uno, I., Chen, X., Yamamoto, S., Zheng, H., Li, J., and Wang, Z.: Importance of

573 mineral dust and anthropogenic pollutants mixing during a long-lasting high PM event over East
 574 Asia, *Environ. Pollut.*, 234, 368–378, <https://doi.org/10.1016/j.envpol.2017.11.068>, 2018.

575 Weber, R.; Guo, H.; Russell, A.; Nenes, A.: High aerosol acidity despite declining atmospheric sulfate
 576 concentrations over the past 15 years, *Nature Geoscience.*, 9, 282–285,
 577 <https://doi.org/10.1038/ngeo2665>, 2016.

578 Wei, Y.; Wang, S.; Jiang, N.; Zhang, R.; and Hao, Q. Comparative multi-model study of PM_{2.5} acidity
 579 trend changes in ammonia-rich regions in winter: Based on a new ammonia concentration
 580 assessment method, *J. Hazard.*, 458, 15, <https://doi.org/10.1016/j.jhazmat.2023.131970>,
 581 2023.

582 Wen, L., Xue, L., Wang, X., Xu, C., Chen, T., Yang, L., Wang, T., Zhang, Q., and Wang, W.:
 583 Summertime fine particulate nitrate pollution in the North China Plain: increasing trends,
 584 formation mechanisms and implications for control policy, *Atmos. Chem. Phys.*, 18, 11261–
 585 11275, <https://doi.org/10.5194/acp-18-11261-2018>, 2018.

586 Wexler, A. S. and Seinfeld, J. H.: Second-generation inorganic aerosol model, *Atmos. Environ., Part*
 587 *A. General Topics*, 25, 2731–2748, [https://doi.org/10.1016/0960-1686\(91\)90203-J](https://doi.org/10.1016/0960-1686(91)90203-J), 1991.

588 Xie, Y., Wang, G., Wang, X., Chen, J., Chen, Y., Tang, G., Wang, L., Ge, S., Xue, G., Wang, Y., and
 589 Gao, J.: Nitrate-dominated PM_{2.5} and elevation of particle pH observed in urban Beijing during
 590 the winter of 2017, *Atmos. Chem. Phys.*, 20, 5019–5033, [https://doi.org/10.5194/acp-20-5019-](https://doi.org/10.5194/acp-20-5019-2020)
 591 [2020](https://doi.org/10.5194/acp-20-5019-2020), 2020.

592 Xu, K., Yin, L., Chen, Q., Liao, D., Ji, X., Zhang, K., Wu, Y., Xu, L., Li, M., Fan, X., Zhang, F., Huang,
 593 Z., Chen, J., and Hong, Y.: Quantitative analysis of influencing factors to aerosol pH and its
 594 responses to PM_{2.5} and O₃ pollution in a coastal city, *J. Environ. Sci.*, 151, 284–297,
 595 <https://doi.org/10.1016/j.jes.2024.03.044>, 2025.

596 Yu, F., Yan, Q., Jiang, N., Su, F., Zhang, L., Yin, S., Li, Y., Zhang, R., and Chen, L.: Tracking pollutant
 597 characteristics during haze events at background site Zhongmu, Henan Province, China, *Atmos.*
 598 *Pollut. Res.*, 8, 64–73, <https://doi.org/10.1016/j.apr.2016.07.005>, 2017.

599 Zhai, S.; Jacob, D.J.; Wang, X.; Shen, L.; Li, K.; Zhang, Y.; Gui, K.; Zhao, T.; Liao, H. Fine particulate
 600 matter (PM_{2.5}) trends in China, 2013–2018: separating contributions from anthropogenic

emissions and meteorology, *Atmos. Chem. Phys.*, 19, 11031–11041, <https://doi.org/10.5194/acp-19-11031-2019>, 2019.

Zhang, B., Shen, H., Liu, P., Guo, H., Hu, Y., Chen, Y., Xie, S., Xi, Z., Skipper, T. N., and Russell, A. G.: Significant contrasts in aerosol acidity between China and the United States, *Atmos. Chem. Phys.*, 21, 8341–8356, <https://doi.org/10.5194/acp-21-8341-2021>, 2021.

Zhang, G., Ding, C., Jiang, X., Pan, G., Wei, X., and Sun, Y.: Chemical compositions and sources contribution of atmospheric particles at a typical steel industrial urban site, *Sci. Rep.*, 10, 7654, <https://doi.org/10.1038/s41598-020-64519-x>, 2020.

Zhang, Z., Dong, Z., Zhang, C., Qian, G., and Lei, C.: The geochemical characteristics of dust material and dust sources identification in northwestern China, *J. Geochem. Explor.*, 175, 148–155, <https://doi.org/10.1016/j.gexplo.2016.11.006>, 2017.

Zhang, Z., Kuang, Z., Yu, C., Wu, D., Shi, Q., Zhang, S., Wang, Z., and Liu, D.: Trans-boundary dust transport of dust storms in Northern China: A study utilizing ground-based lidar network and CALIPSO satellite, *Remote sens.*, 16, 1196, <https://doi.org/10.3390/rs16071196>, 2024.

Zheng, G., Su, H., and Cheng, Y.: Revisiting the key driving processes of the decadal trend of aerosol acidity in the U.S, *Acs. Environ. Au.*, 2, 346–353, <https://doi.org/10.1021/acsenvironau.1c00055>, 2022.

Zheng, G., Su, H., Wang, S., Andreae, M. O., Pöschl, U., and Cheng, Y.: Multiphase buffer theory explains contrasts in atmospheric aerosol acidity, *Science.*, 369, 1374–1377, <https://doi.org/10.1126/science.aba3719>, 2020.

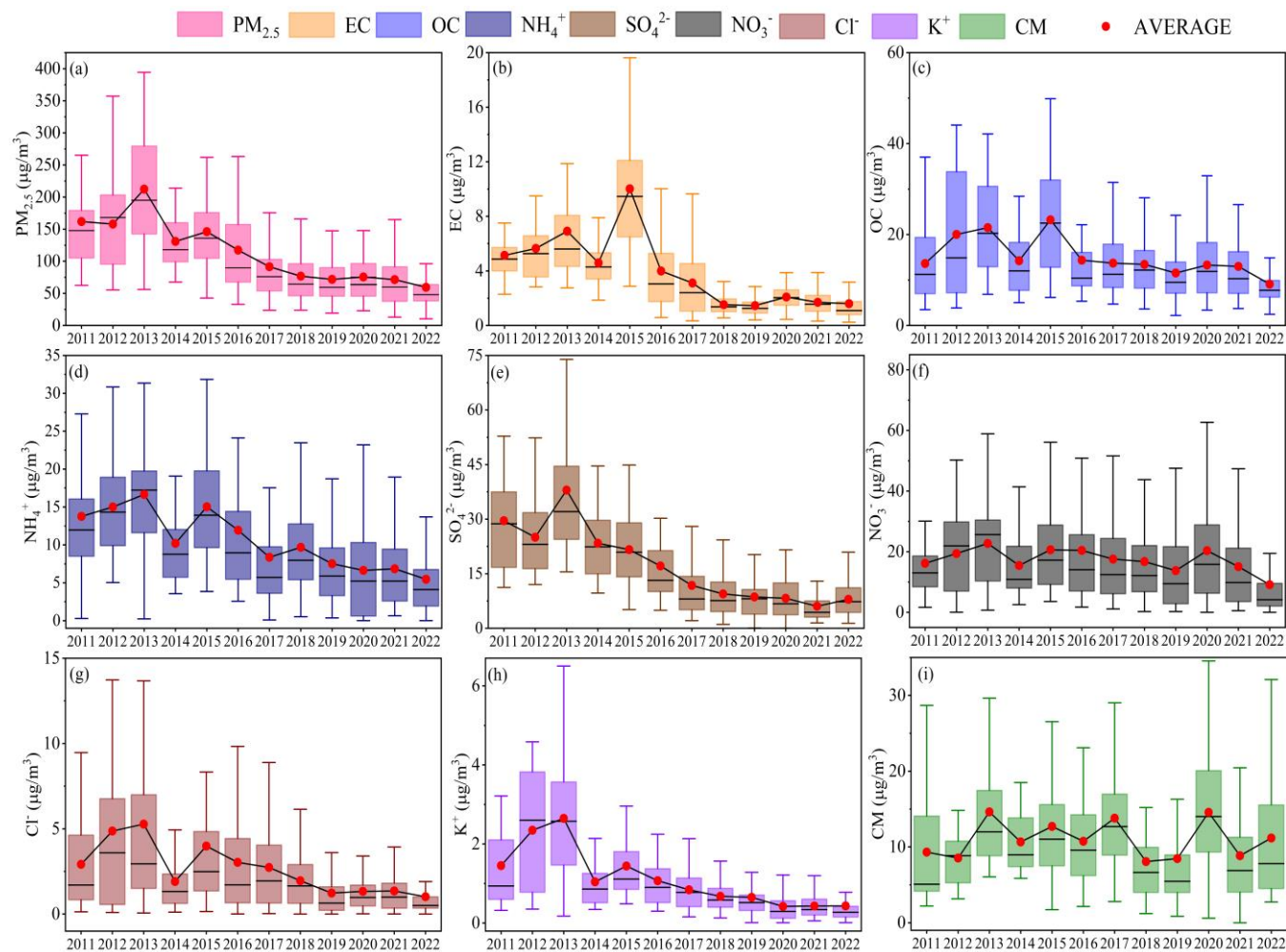
Zhou, M., Zheng, G., Wang, H., Qiao, L., Zhu, S., Huang, D., An, J., Lou, S., Tao, S., Wang, Q., Yan, R., Ma, Y., Chen, C., Cheng, Y., Su, H., and Huang, C.: Long-term trends and drivers of aerosol pH in eastern China, *Atmos. Chem. Phys.*, 22, 13833–13844, <https://doi.org/10.5194/acp-22-13833-2022>, 2022.

Zhou, W., Gao, M., He, Y., Wang, Q., Xie, C., Xu, W., Zhao, J., Du, W., Qiu, Y., Lei, L., Fu, P., Wang, Z., Worsnop, D. R., Zhang, Q., and Sun, Y.: Response of aerosol chemistry to clean air action in Beijing, China: Insights from two-year ACSM measurements and model simulations, *Environ Pollut.*, 255, 113345, <https://doi.org/10.1016/j.envpol.2019.113345>, 2019.

629 Zuend, A. and Seinfeld, J. H.: Modeling the gas-particle partitioning of secondary organic aerosol: the
630 importance of liquid-liquid phase separation, *Atmos. Chem. Phys.*, 12, 3857–3882,
631 <https://doi.org/10.5194/acp-12-3857-2012>, 2012.

632 Zuend, A., Marcolli, C., Peter, T., and Seinfeld, J. H.: Computation of liquid-liquid equilibria and phase
633 stabilities: implications for RH-dependent gas/particle partitioning of organic-inorganic aerosols,
634 *Atmos. Chem. Phys.*, 10, 7795–7820, <https://doi.org/10.5194/acp-10-7795-2010>, 2010.

635



637
638 **Figure 1. Long-term trends in the concentrations of $PM_{2.5}$ and its chemical components in from 2011**
639 **to 2022 in Zhengzhou. Box plots depict annual averages (red dots) and medians (black lines), the top,**
640 **middle, and bottom lines represent the 75, 50, and 25 percentiles of statistical data, respectively, and**
641 **the upper and lower whiskers represent the 90 and 10 percentiles of statistical data, respectively.**

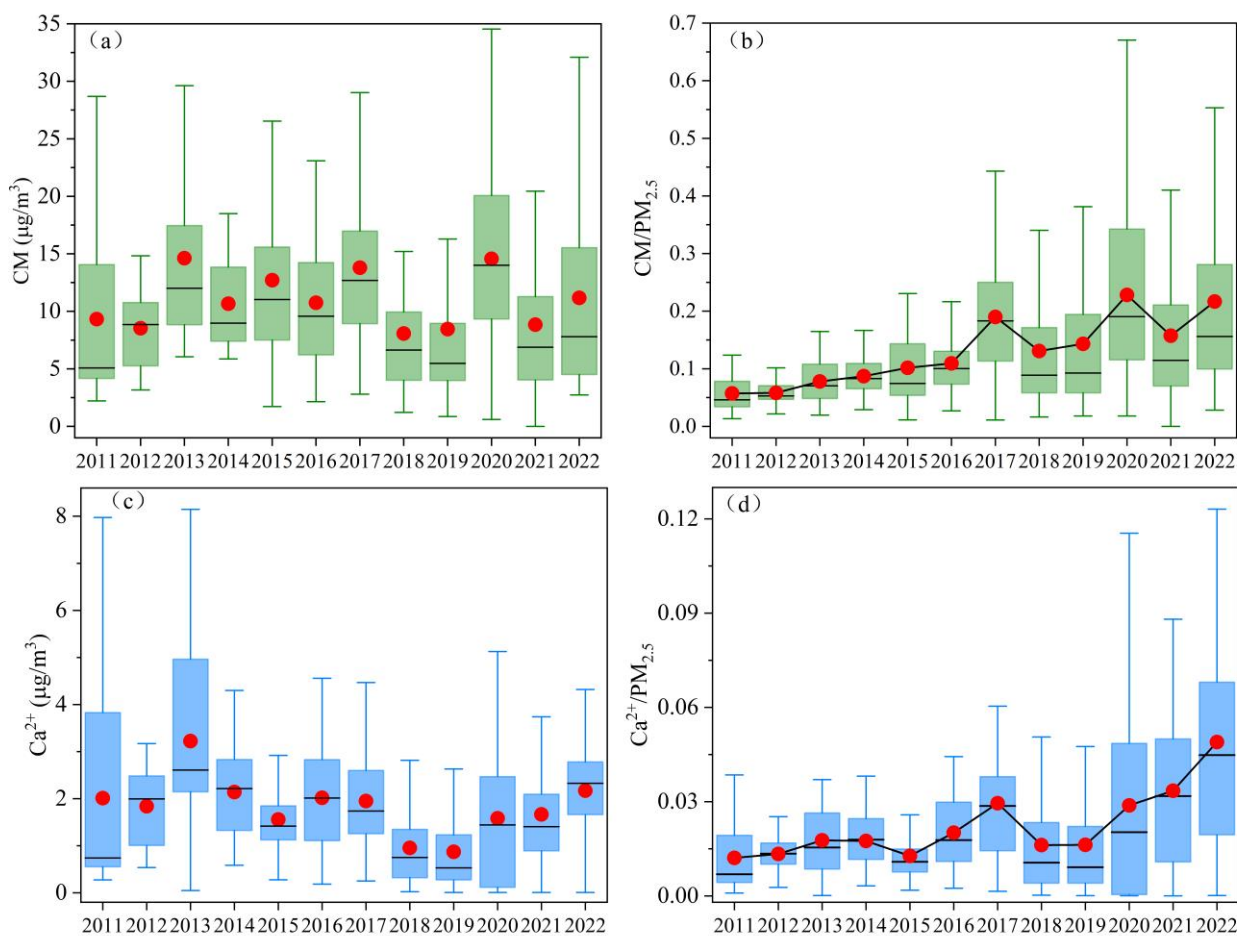


Figure 2. (a) and (c) Long-term trends in CM and Ca^{2+} concentrations in Zhengzhou from 2011 to 2022, respectively. Box plots depict annual averages (red dots) and medians (black lines). (b) and (d) Long-term trends in the proportions of CM and Ca^{2+} in $\text{PM}_{2.5}$, respectively.

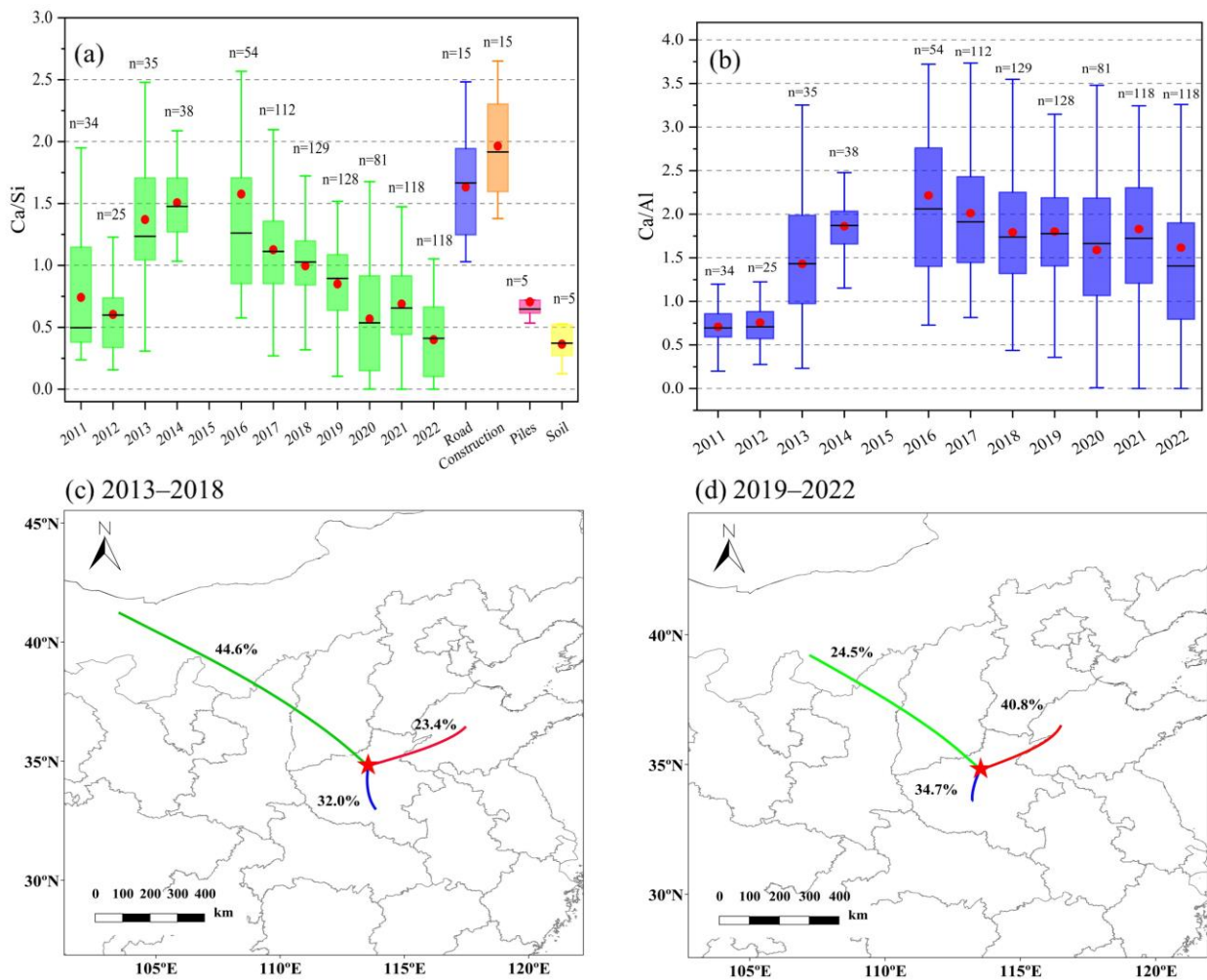


Figure 3. (a) The annual Ca/Si ratios in Zhengzhou from 2011 to 2022 compared with those in various dust sources (specific values and references in Table S5). The red dots and black lines in the box plots represent the annual averages and medians, respectively, with n indicating the sample size. (b) The Ca/Al ratios in Zhengzhou from 2011 to 2022. The red dots and black lines in the box plots represent the annual averages and medians, respectively, with n indicating the sample size. (c) and (d) The transport pathways of CM during 2013–2018 and 2019–2022, respectively.

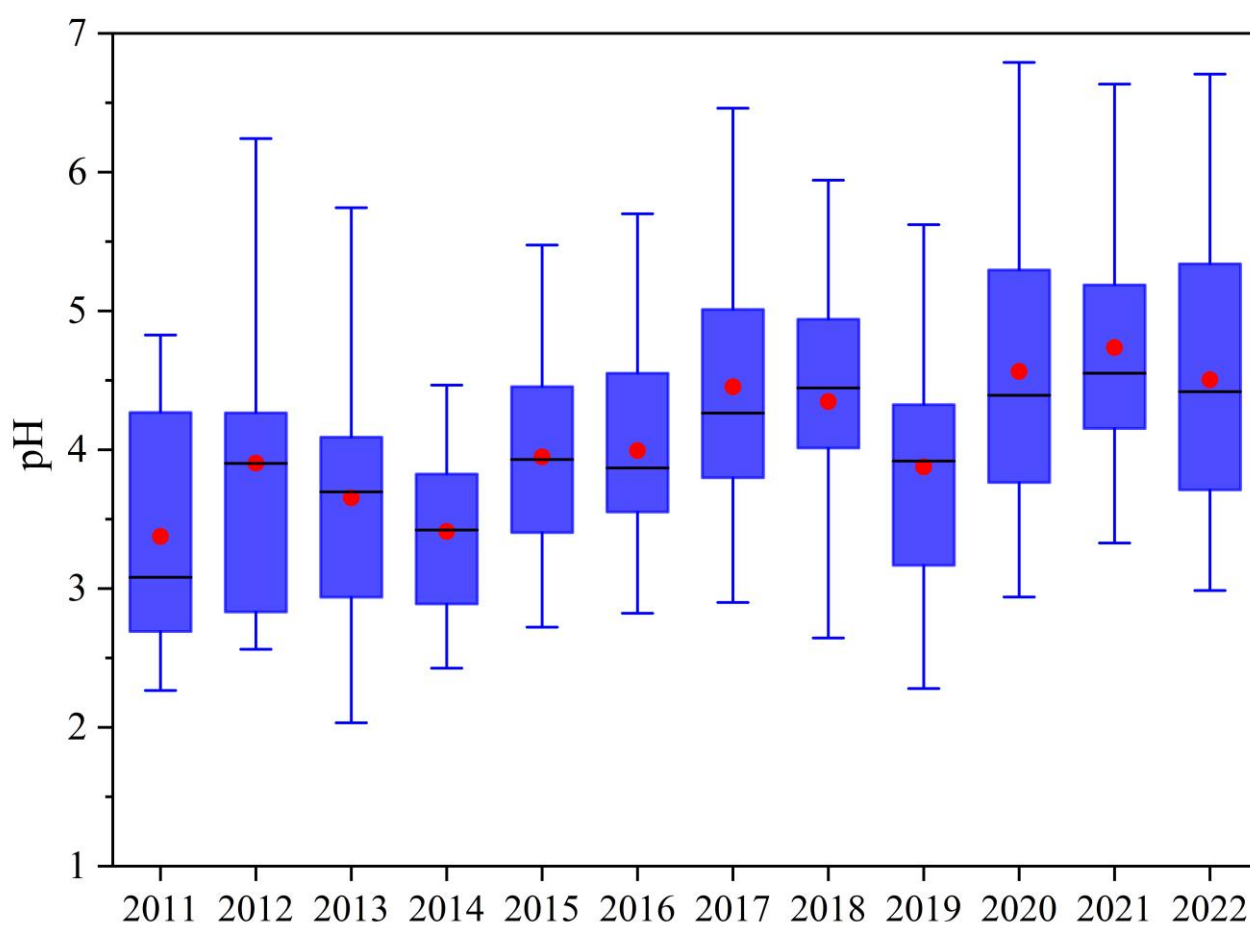


Figure 4. The time series of particle pH in Zhengzhou from 2011 to 2022. In the boxplots, red dots and black lines represent the annual mean and median values, respectively.

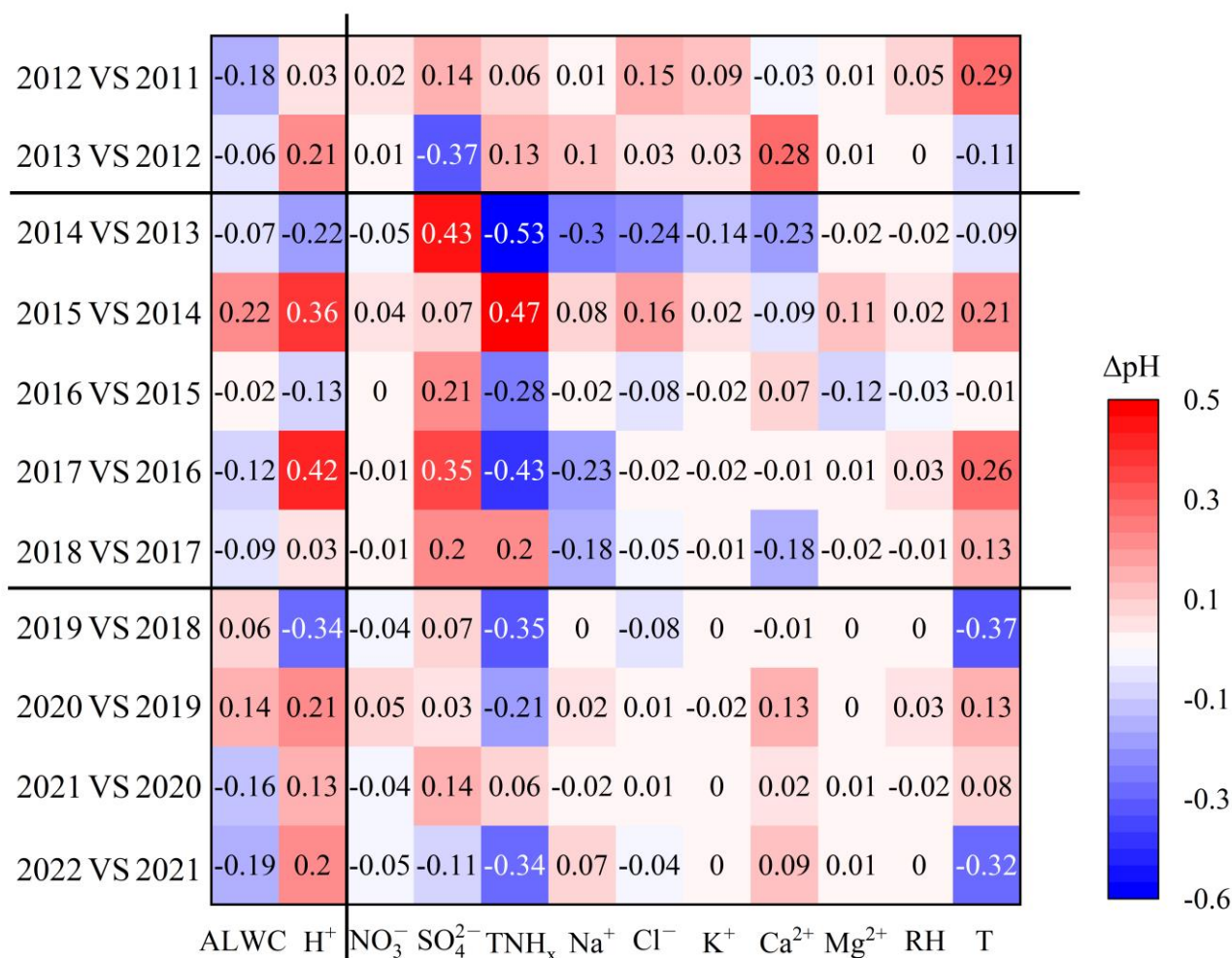


Figure 5. Contribution of each component to the changes in pH (ΔpH) between adjacent years. The difference between component concentrations and meteorological parameters between adjacent years is listed in Table S6.

660 **Table**

661 **Table 1. Annual average concentrations of PM_{2.5} and its components from 2011 to 2022 in Zhengzhou, China (μg/m³).**

Years	PM _{2.5}	EC	OC	NO ₃ ⁻	SO ₄ ²⁻	NH ₄ ⁺	CM	Ca ²⁺
2011	161.9 ± 81.4	5.1 ± 2.1	13.6 ± 8.6	16.2 ± 11.2	29.6 ± 14.3	13.8 ± 8.3	9.3 ± 7.3	2.0 ± 2.2
2012	157.9 ± 71.2	5.6 ± 2.5	20.0 ± 13.4	20.2 ± 13.7	25.0 ± 11.2	15.0 ± 7.1	8.5 ± 3.4	1.8 ± 0.8
2013	212.4 ± 101.5	6.9 ± 3.8	21.5 ± 10.4	22.7 ± 13.2	38.0 ± 19.9	17.1 ± 6.9	14.6 ± 8.3	3.2 ± 2.1
2014	130.8 ± 48.7	4.6 ± 2.0	14.2 ± 8.2	15.5 ± 10.8	23.4 ± 9.3	10.2 ± 6.2	10.7 ± 4.4	2.1 ± 1.0
2015	146.1 ± 61.0	10.0 ± 4.7	23.2 ± 11.6	20.6 ± 14.5	21.6 ± 9.8	15.7 ± 7.5	12.7 ± 6.8	1.6 ± 0.7
2016	117.4 ± 73.5	4.0 ± 2.8	14.4 ± 10.0	20.4 ± 18.7	17.1 ± 11.3	11.9 ± 10.6	10.8 ± 5.3	2.0 ± 1.1
2017	91.5 ± 61.1	3.1 ± 2.5	13.7 ± 7.5	17.6 ± 15.9	11.8 ± 11.6	8.4 ± 7.9	13.8 ± 6.5	2.0 ± 1.0
2018	76.8 ± 41.6	1.5 ± 0.7	13.4 ± 7.3	16.7 ± 13.5	9.4 ± 6.0	9.7 ± 6.1	8.1 ± 5.7	1.0 ± 0.8
2019	68.4 ± 34.8	1.5 ± 0.8	11.5 ± 6.8	13.8 ± 13.9	8.6 ± 6.4	7.5 ± 6.1	8.5 ± 7.8	0.9 ± 0.9
2020	75.5 ± 31.8	2.1 ± 0.9	13.3 ± 7.9	18.6 ± 14.2	8.3 ± 5.6	6.7 ± 6.6	14.6 ± 7.6	1.6 ± 1.4
2021	71.5 ± 45.9	1.7 ± 0.9	13.0 ± 8.0	15.1 ± 15.1	6.1 ± 4.5	6.8 ± 6.0	8.9 ± 7.0	1.7 ± 1.2
2022	59.5 ± 41.1	1.6 ± 1.5	9.1 ± 8.1	10.0 ± 14.4	7.9 ± 4.5	5.5 ± 5.4	11.2 ± 8.3	2.2 ± 1.1

662

Supplement materials:

Text S1 Instruments and Measurements.

Samples were collected using a high-volume sampler (TE-6070D, Tisch, USA) and air particulate samplers (TH-16A, Tianhong, China) from April 2011 to December 2022. Two quartz filters and two Teflon filters were used daily from 10:00 AM to 9:00 AM the next day, resulting in a total of 5848 samples. After excluding abnormal data due to instrument malfunctions, 4228 valid samples were obtained. Detailed information on the samples is provided in Table S1.

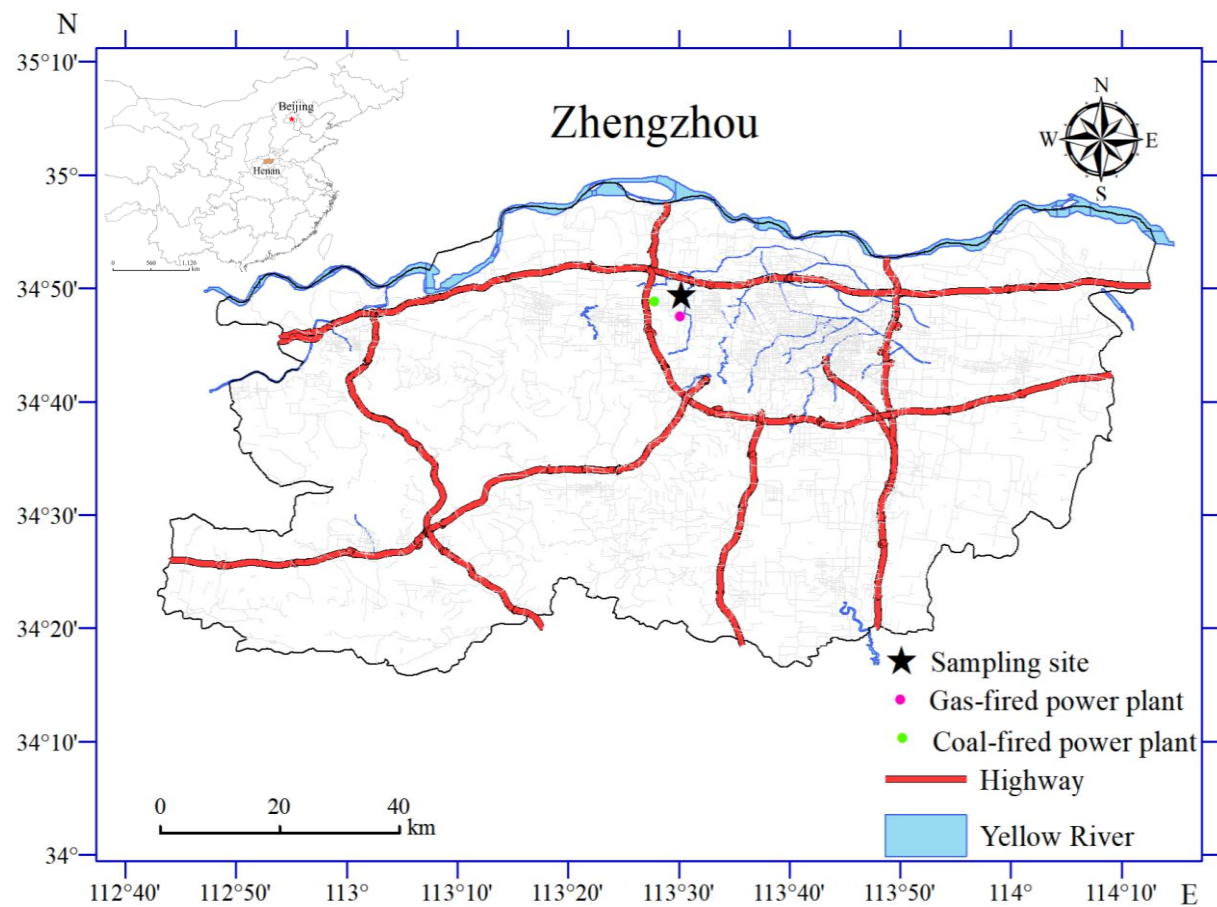
Organic carbon (OC) and elemental carbon (EC) were analyzed using a carbon analyzer (Model 5L, Sunset Laboratory, USA). The analysis of EC and OC was conducted in two stages. In the first stage, the filter membrane was placed in a quartz heating furnace under a pure helium atmosphere. As the temperature gradually increased to approximately 580°C, OC was volatilized and released. In the second stage, heating continued in a mixed atmosphere of 2% oxygen and 98% helium. When the temperature reached approximately 870°C, EC underwent oxidative decomposition and was released. During the helium flow transmission, OC and EC released at different temperatures were completely oxidized to CO₂ in a MnO₂ oxidation furnace and subsequently reduced to CH₄ for detection by a flame ionization detector (FID). The detection limits for both OC and EC were 0.2 µg/cm². Before each sample analysis, calibration was performed using a standard sucrose solution. Additionally, parallel tests were conducted every ten samples to ensure accuracy.

Water-soluble inorganic ions (Cl⁻, NO₃⁻, SO₄²⁻, Na⁺, NH₄⁺, K⁺, Mg²⁺, and Ca²⁺) were measured using ion chromatography (ICS-90 and ICS-900 models, Dionex, USA). Half of the PM_{2.5} filter was

683 cut into pieces and ultrasonically extracted with 20 mL of Milli-Q water for 30 min, followed by
684 filtering through a 0.45 mm polytetrafluoroethylene syringe filter before analysis. The cation
685 concentrations were determined by an IonPacASII-HC4 mm anion separation column and an
686 IonPacAGII-HC4 mm guard column, with 20 mM methane sulfonate as an eluent at 0.8 mL/min. The
687 anions were measured by an IonPacCS12A cation separation column and an IonPacCG12A guard
688 column, with a solution of 8.0 mM Na₂CO₃ + 1.0 mM NaHCO₃ as an eluent at 1.0 mL/min. The
689 regression coefficients (R^2) of the calibration curves were over 0.9996 for all ions, except NH₄⁺
690 (0.9988), which showed a quadratic response.

691 Elements were analyzed using a wavelength dispersive X-ray fluorescence spectrometer (S8
692 TIGER, Bruker, Germany) to determine concentrations of Fe, Na, Mg, Al, Si, Cl, K, Ca, V, Ni, Cu, Zn,
693 Cr, Mn, Co, Cd, Ga, As, Se, Sr, Sn, Sb, Ba, and Pb (Tremper et al., 2018), which has been approved
694 by the United States Environmental Protection Agency (Chow and Watson, 1994). The spectrometer
695 was equipped with an X-ray tube featuring close coupling among the tube, sample, and detector,
696 ensuring high efficiency and optimal excitation of elements within the sample. Before analysis, the
697 instrument was calibrated using a series of high-quality, self-prepared standards. Calibration
698 procedures were conducted following established methods (Chow and Watson, 1994). To assess
699 potential contamination and ensure data quality, blank filters were routinely analyzed alongside each
700 batch of samples.

701



703
704 **Figure S1. Sampling site in Zhengzhou, China. © 2019 National Geomatics Center of China. All**
705 **rights reserved.**
706

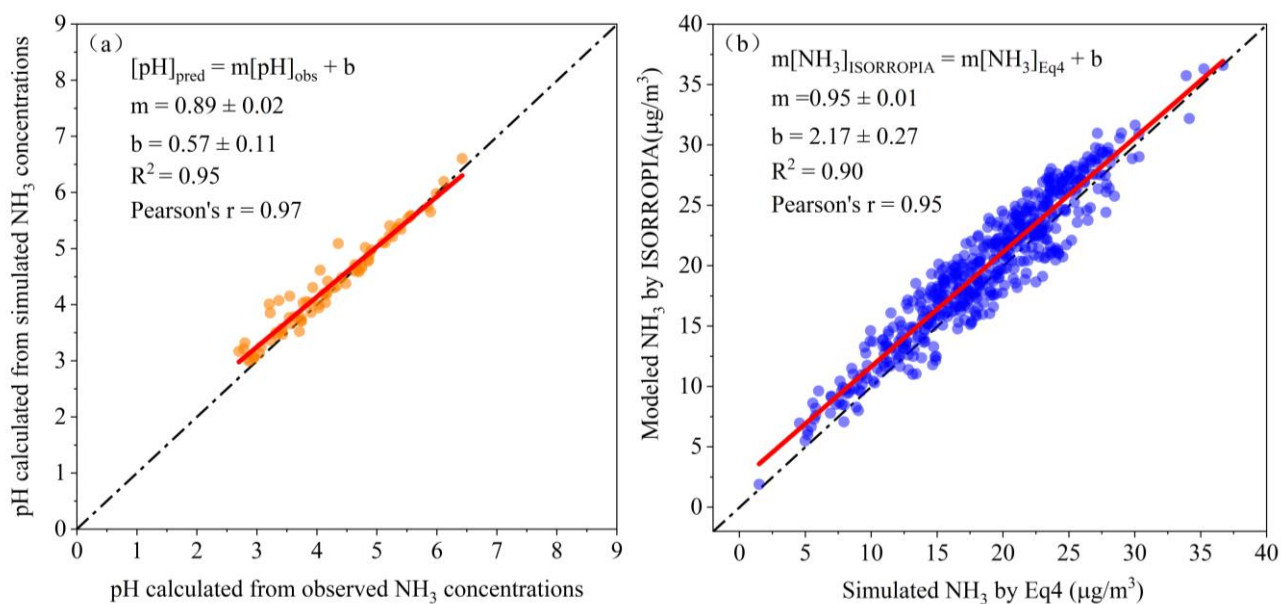


Figure S2. Verification of the NH₃ Method.

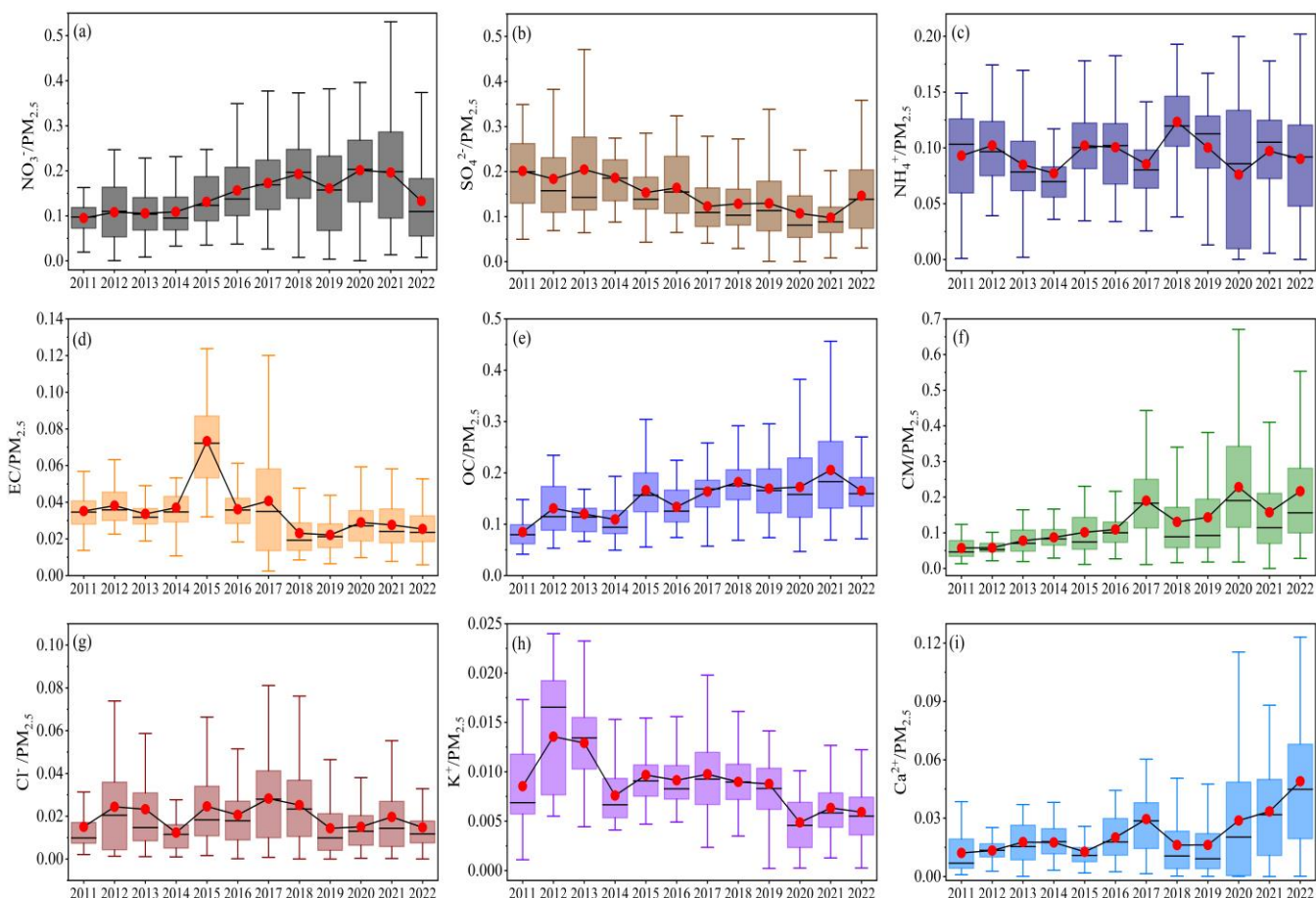


Figure S3. Trends in the proportions of chemical components in PM_{2.5} from 2011 to 2022.

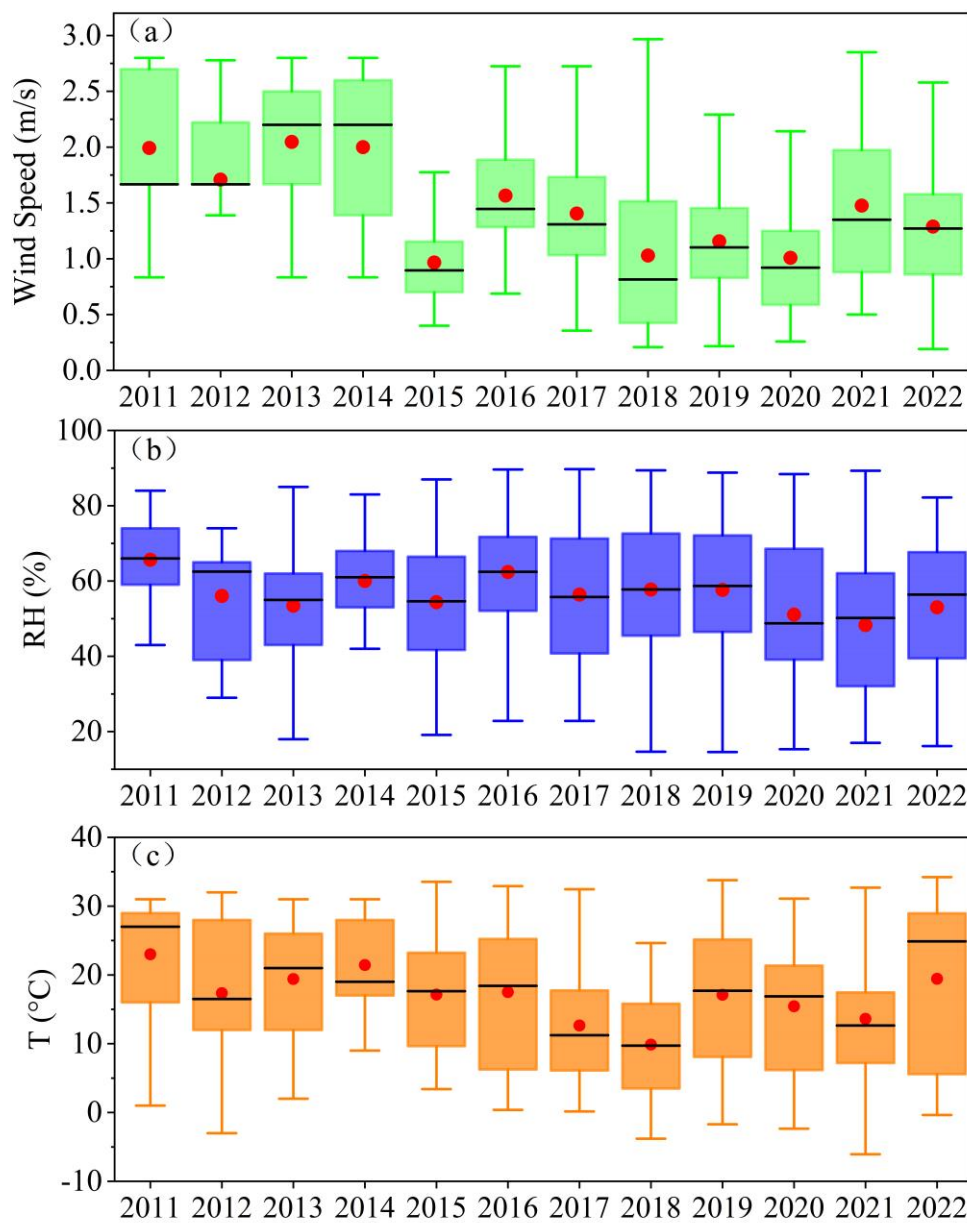


Figure S4. Trends in the meteorological parameters from 2011 to 2022.

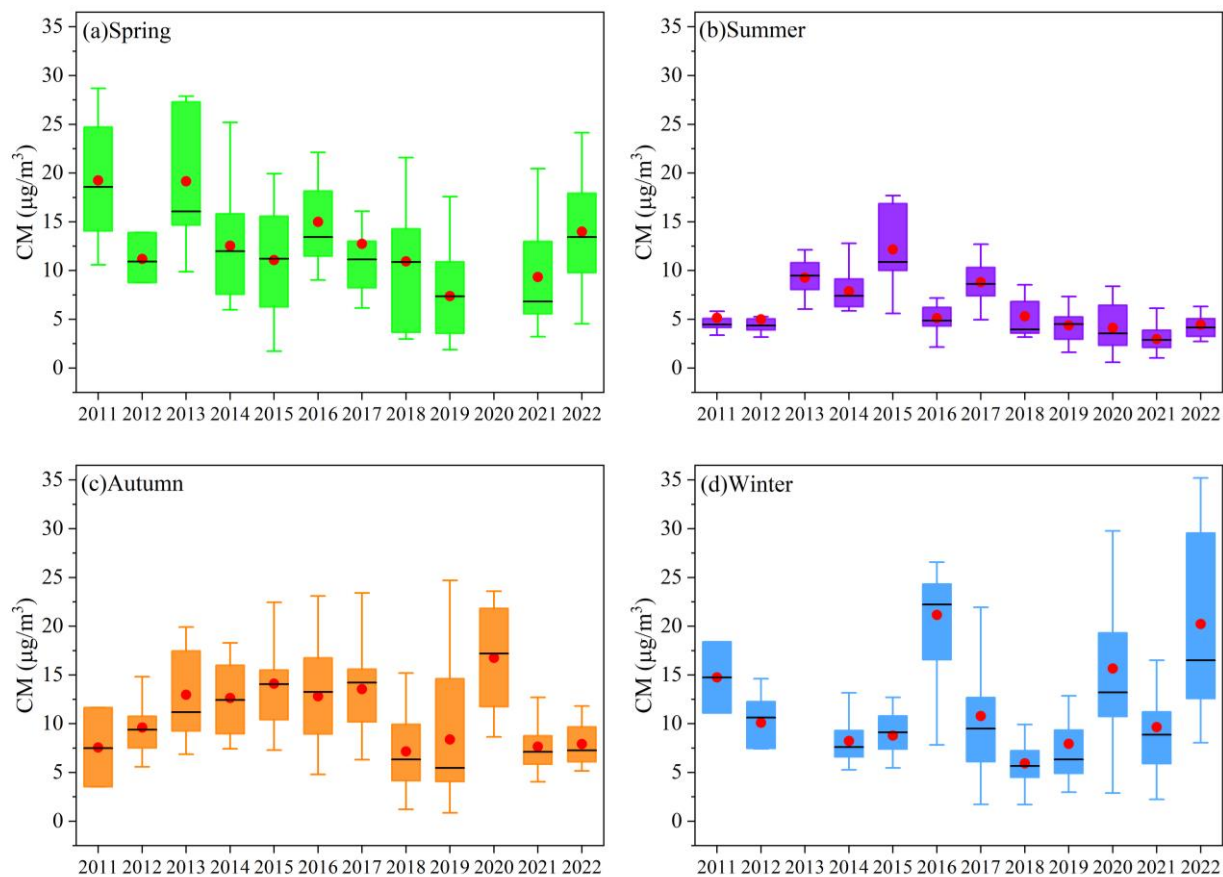


Figure S5. Trends in the CM concentrations in different seasons from 2011 to 2022.

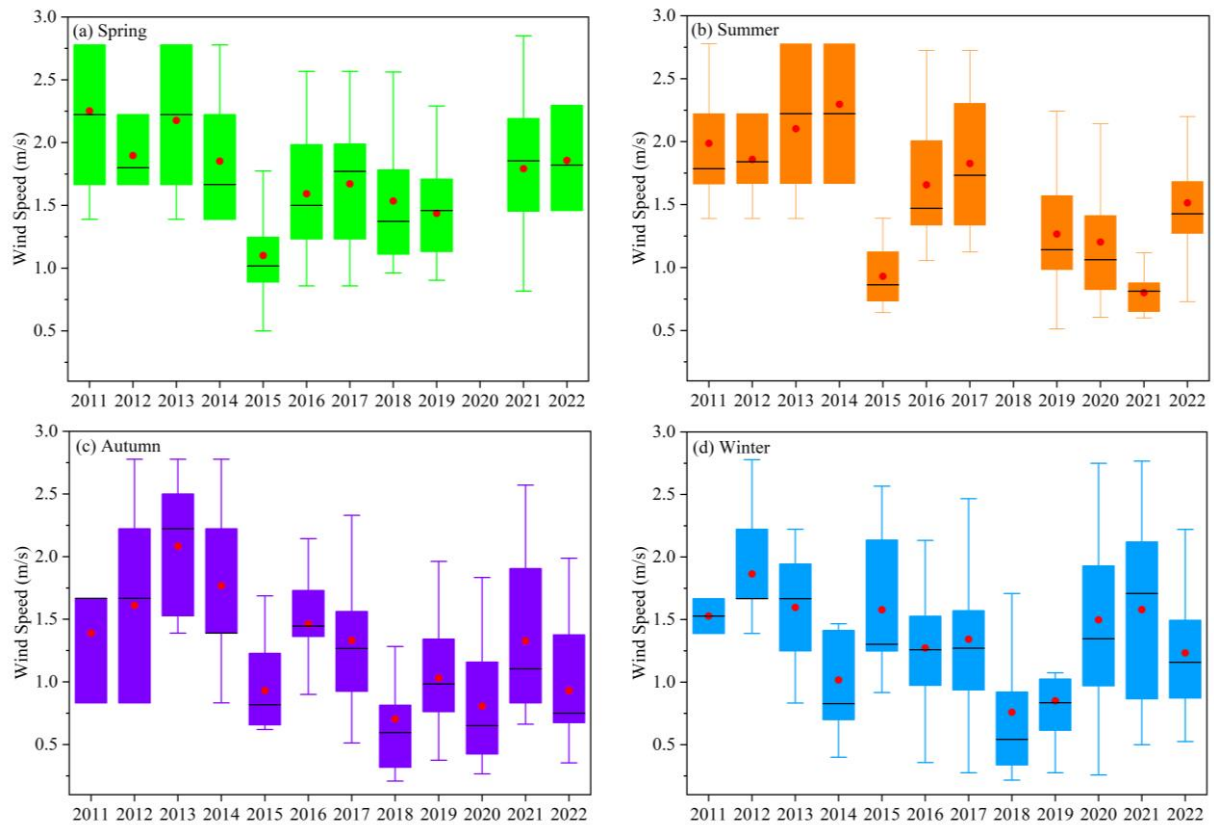


Figure S6. The variation in WS across different seasons from 2011 to 2022.

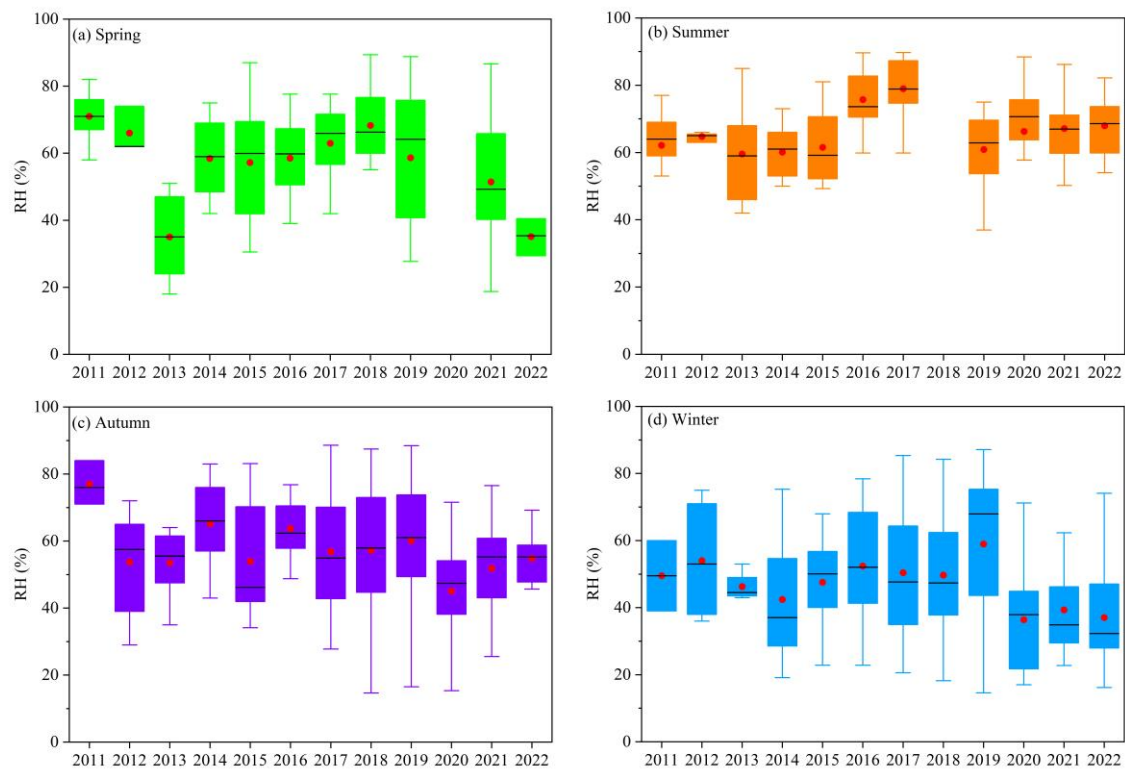


Figure S7. The variation in RH across different seasons from 2011 to 2022.

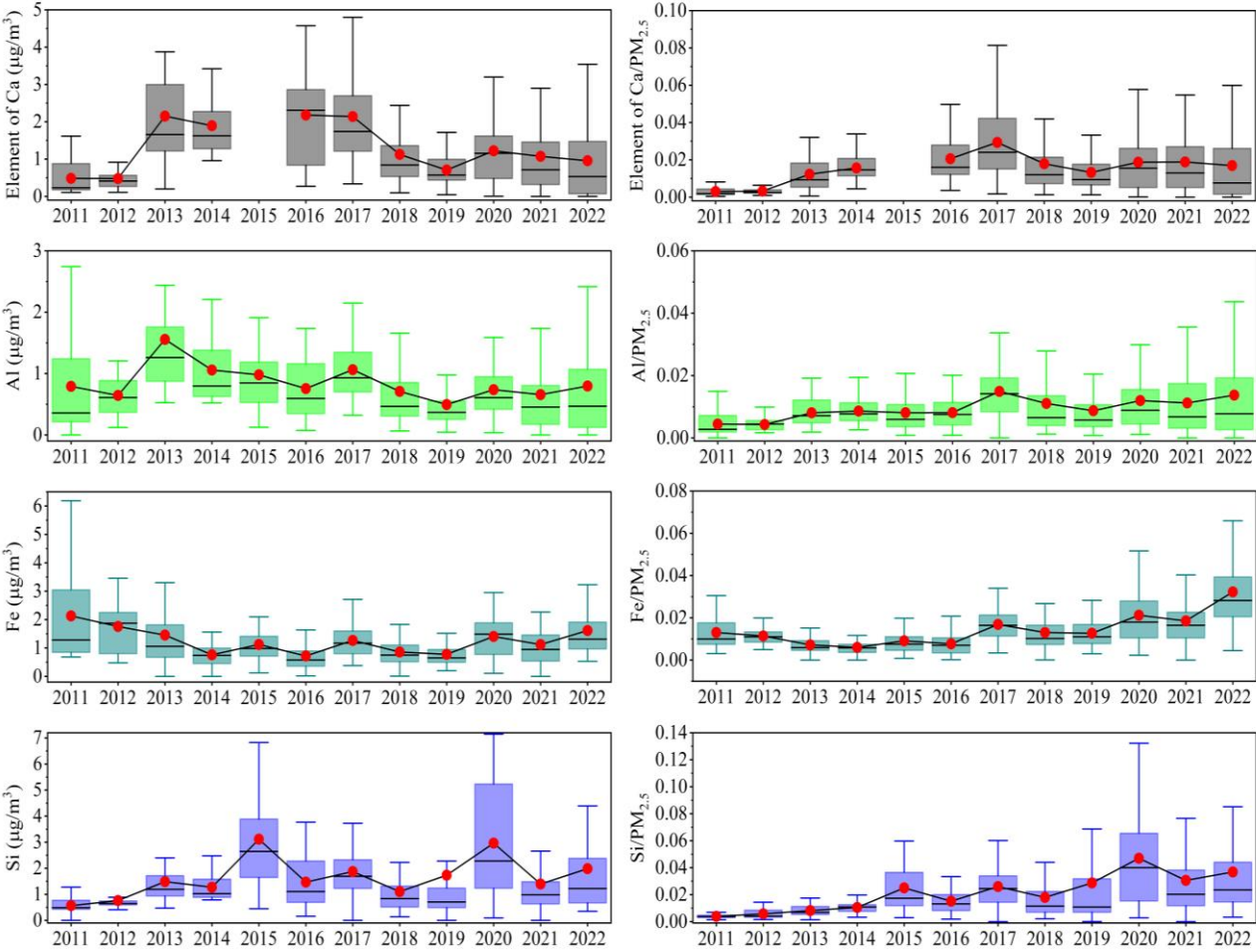


Figure S8. Trends in the concentrations of crustal elements and their proportions in $\text{PM}_{2.5}$ from 2011 to 2022.

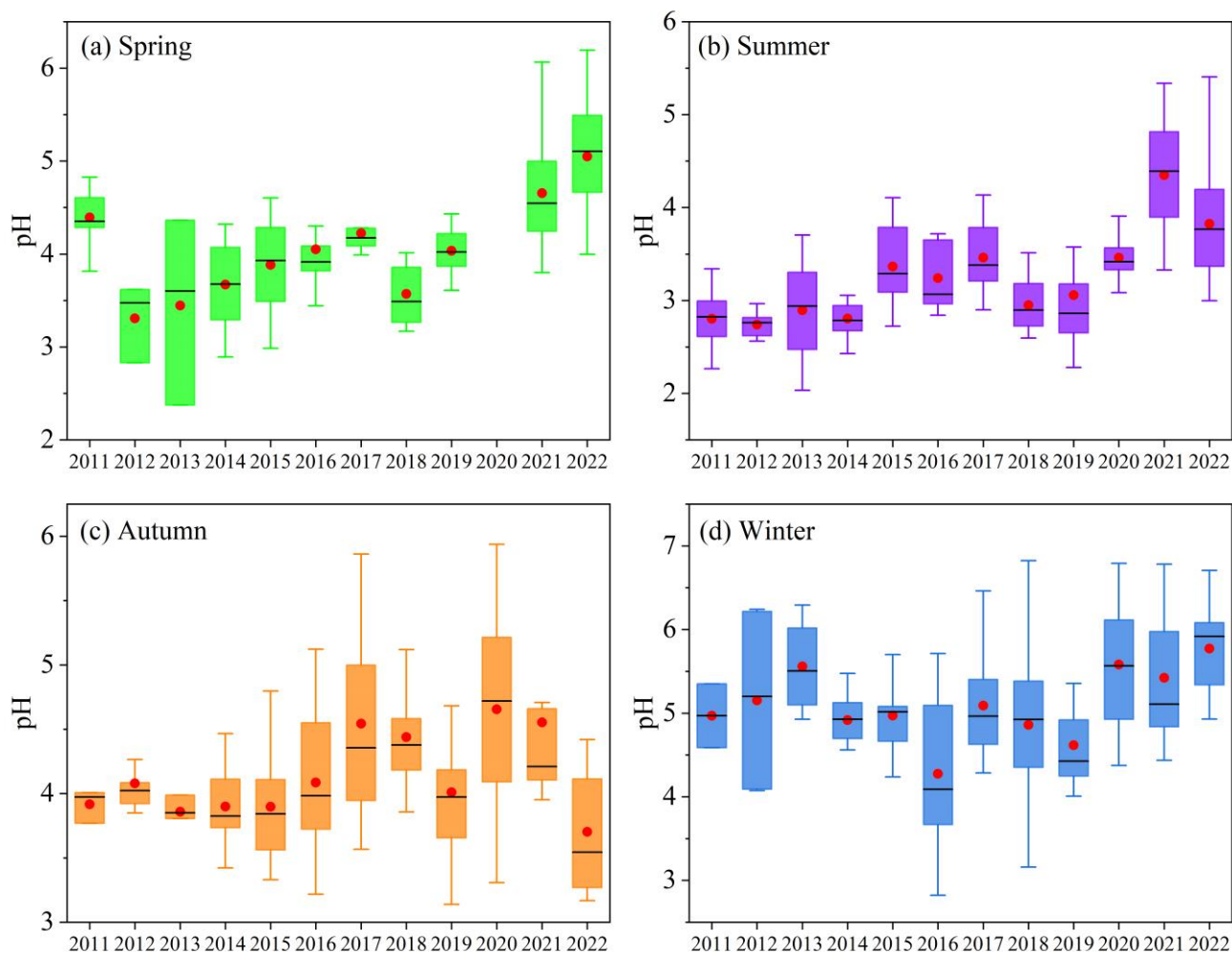


Figure S9. Trends in the particle pH in different seasons from 2011 to 2022.

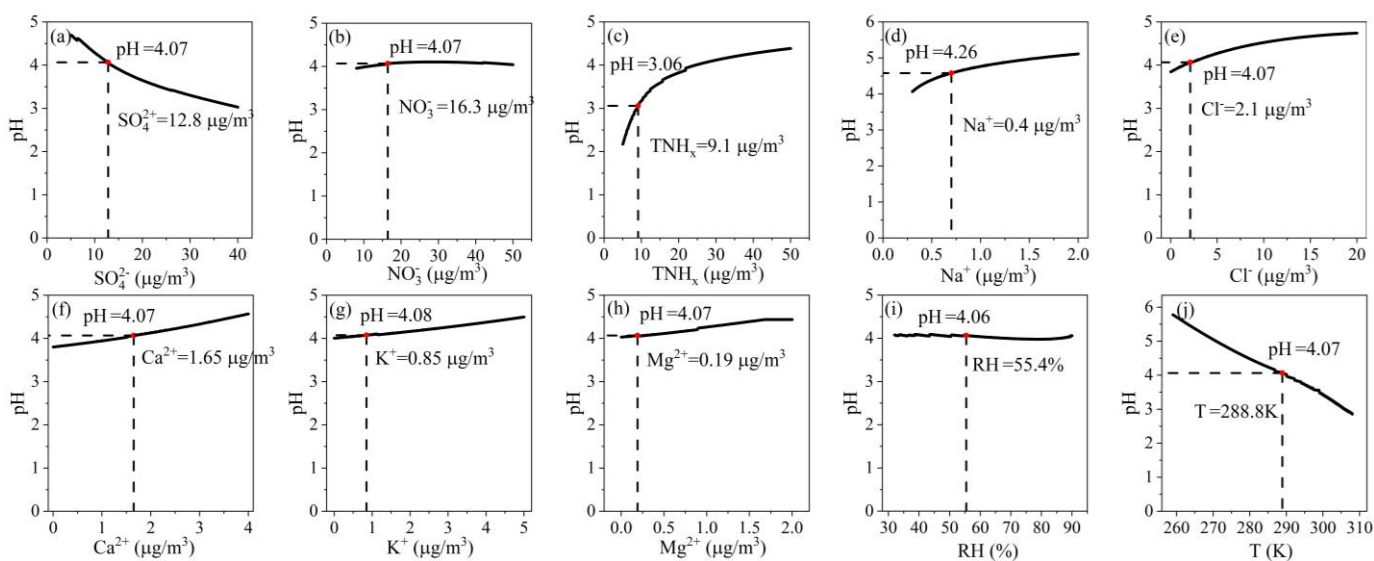


Figure S10. Sensitivity analysis of input parameters to particle pH. The dashed line represents the average of the observational data from 2011 to 2022.

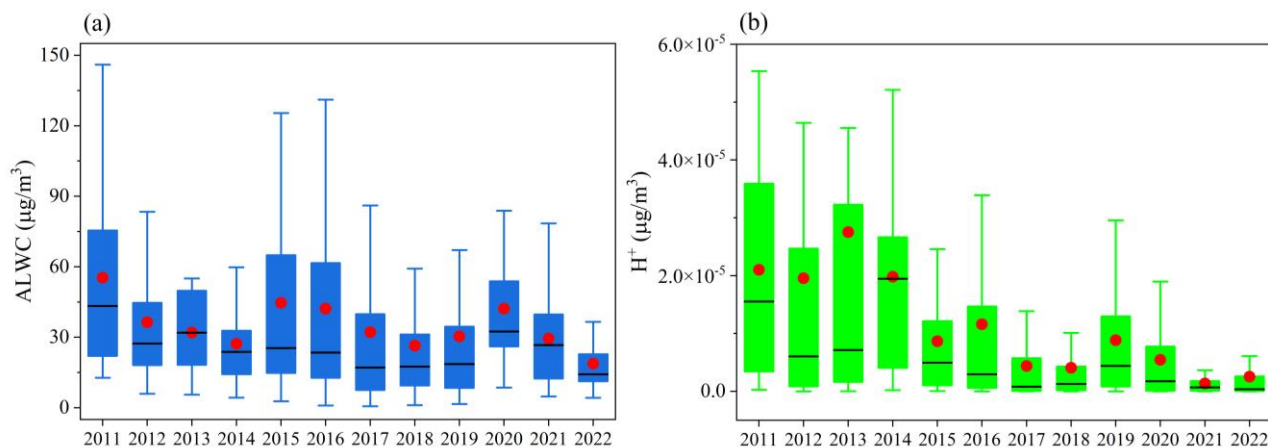


Figure S11. Trends in aerosol liquid water content (ALWC) and H^+ concentrations from 2011 to 2022

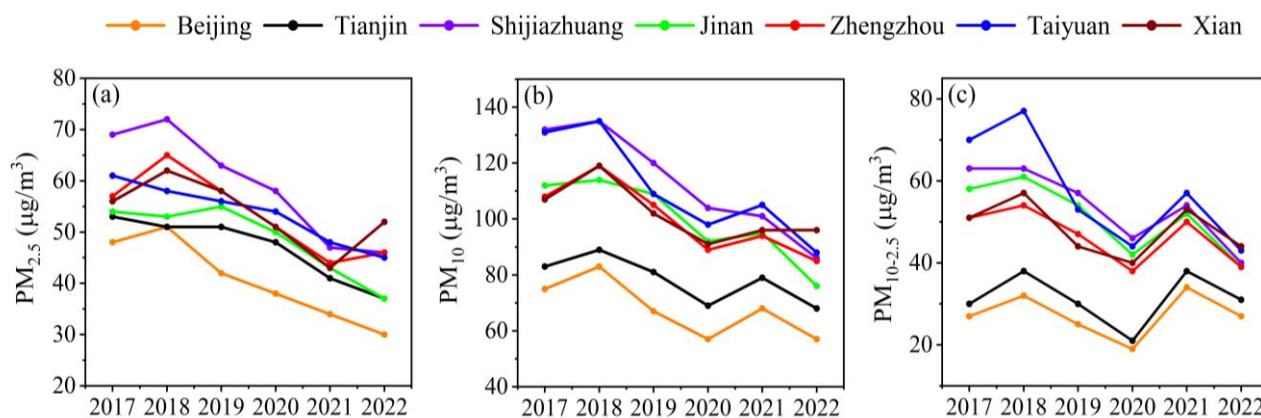


Figure S12. Trends in the annual average concentrations of $\text{PM}_{2.5}$, PM_{10} , and $\text{PM}_{10-2.5}$ in provincial capitals in the North China Plain.

747 Table S1. Information on sampling date and numbers.

Years	Sampling date	The effective number of samples
2011	April 7–20	188
	July 1–31	
	October 28–December 2	
	December 11–November 23	
2012	February 25–26	140
	April 21–May 6	
	July 22–August 2	
	October 17–November 1	
	December 8–25	
2013	February 25–March 6	184
	April 1–May 1	
	June 5–July 30	
	September 20–October 13	
	December 2–18	
2014	April 1–May 5	180
	June 18–July 20	
	October 7–24	
	December 30–31	
2015	January 1–15	248
	April 1–20	
	July 1–20	
	October 9–24	
2016	January 6–22	252
	April 8–30	
	July 9–31	
	October 1–20	
	December 29–31	
2017	January 1–20	480
	April 18–May 4	
	July 1–26	
	October 14–December 31	
2018	January 1–31	600
	April 1–30	
	July 1–31	
	October 9–December 31	

2019	January 1–31	592
	April 1–30	
	July 1–31	
	September 2–October 31	
	November 12–30	
	December 21–31	
2020	January 1–20	332
	June 5–July 31	
	October 6–November 13	
	December 15–31	
2021	January 1–31	540
	March 16–April 30	
	July 1–August 8	
	October 17–December 31	
2022	January 1–4	492
	April 1–May 3	
	July 1–August 11	
	September 5–October 11	
	December 10–31	
Total		4228

Table S2. The method detection limit (MDL) and measurement uncertainties (Unc) of individual

	components	
	MDLs ($\mu\text{g}/\text{m}^3$)	Unc (%)
EC	0.1	13.1
OC	0.1	9.8
Na ⁺	0.005	9.6
NH ₄ ⁺	0.011	10.1
K ⁺	0.006	9.5
Mg ²⁺	0.002	9.3
Ca ²⁺	0.017	8.8
F ⁻	0.001	8.2
Cl ⁻	0.001	9.3
NO ₃ ⁻	0.015	10.1
SO ₄ ²⁻	0.031	9.9
Na	0.003	10.9
Mg	0.002	10.6
Al	0.004	9.2
Si	0.005	9.3

Cl	0.008	9.5
K	0.005	9.4
Ca	0.01	9.4
V	0.008	57.9
Ni	0.006	96.6
Cr	0.02	24.7
Mn	0.02	16.8
Fe	0.03	9.3
Co	0.009	79.6
Cu	0.005	5.8
Zn	0.003	8.4
Ga	0.005	84.7
As	0.008	27.4
Se	0.006	25.7
Sr	0.006	22.8
Cd	0.03	68.6
Sn	0.02	42.0
Sb	0.02	73.6
Ba	0.02	15.6
Pb	0.02	13.4

753

754

755

756

Table S3. Control measures for dust implemented by Henan Province and Zhengzhou government

Release time	Policies	Regulatory focus
2013.9	Regulations on Reducing Pollutant Emissions in Henan Province	Road, Construction
2014.8	Temporary Regulations on Dust Control Management at Construction Sites in Henan Province	Construction
2016.7	Implementation Plan for Controlling Dust Pollution in Henan Province	Road, Construction
2018.2	Regulations on the Prevention and Control of Atmospheric Pollution in Henan Province	Road, Construction, Piles
2019.4	Special Action Plan for Fine Management of Dust Pollution Prevention and Control at Construction Sites in Zhengzhou City, 2019	Construction

2019.8	Enhanced Action Plan for Intensive Dust Control at Construction Sites in 2019	Construction
2021.1	Special Governance Plan for Key Project Dust Pollution in Zhengzhou	Road, Construction, Piles

757

758

Table S4. Analysis of the inter - annual trends of CM and Ca²⁺ concentrations and pH during different periods using multiple methods.

	2011–2013			2013–2019			2019–2022		
	CM	Ca ²⁺	pH	CM	Ca ²⁺	pH	CM	Ca ²⁺	pH
MK-Z	3.01	2.70	1.41	-9.74	-13.62	3.00	2.48	8.21	5.12
MK- <i>p</i>	0.003	0.007	0.159	<2.2 E-16	<2.2E-16	0.003	0.013	2.20E-16	2.99E-07
Sen's slope	0.082	0.023	7.10E-03	-0.015	-4.14E-03	9.15E-04	5.80E-03	5.42E-03	2.93E-03
LS slope	2.65	0.61	/	-0.81	-0.32	0.11	0.24	0.40	0.21

** MK-Z and MK-*p* represent the trend (Z) and significance (*p*) calculated by the Mann - Kendall method using daily data, respectively; Sen's

slope represents the Sen slope using daily data; LS slope represents the Least - Squares slope using annual data. All the above calculations were

performed using the R language (R version 4.0.2).

Table S5. The ratios of Ca/Si in the source spectrum of different dust sources in China

Dust source	City	Ca/Si	Reference
Road dust	Xi'an	2.04	http://www.klcp.ac.cn/wgPMzypfypk/ycy/201706/t20170610_375562.html
	Yinchuan	2.48	
	Lanzhou	1.67	
	Beijing	1.25	
	Tianjin	1.03	
	Baoding	1.16	
	Shijiazhuang	1.98	
	Handan	1.83	
	Shenyang	1.81	
	Changsha	1.92	
	Chongqing	1.38	
	Chengdu	1.17	
	Kunming	1.94	
	Taiyuan	1.55	
	Nanjing	1.28	
Construction dust	Xi'an	1.69	http://www.klcp.ac.cn/wgPMzypfypk/ycy/201706/t20170610_375562.html
	Yinchuan	1.84	
	Lanzhou	2.33	
	Beijing	2.65	
	Tianjin	1.46	
	Baoding	1.58	
	Shijiazhuang	1.38	
	Handan	1.86	
	Shenyang	1.92	
	Changsha	2.30	
	Chongqing	2.52	
	Chengdu	2.15	
	Kunming	1.60	
	Taiyuan	1.92	
	Nanjing	2.26	
Piles dust	Xi'an	0.72	(Yang, 2016)
	Tianjin	0.57	(Zhang et al., 2018)
	Taiyuan	0.61	(Bi et al., 2007)
	Jinan	1.01	(Bi et al., 2007)
	/	0.65	http://www.nkspap.com:9091/Index.aspx
Soil dust	Nanchang	0.37	(Xu et al., 2019)
	Xi'an	0.27	(Yang, 2016)
	Jincheng	0.13	(Wang et al., 2016)
	Wuhan	0.52	(Gong and Luo, 201

	8)
/	0.53
	http://www.nkspap.com: 9091/Index.aspx

766

Table S6. The difference between component concentrations ($\mu\text{g}/\text{m}^3$) and meteorological parameters between adjacent years.

Years	ALWC	$\text{H}^+(10^{-6})$	NO_3^-	SO_4^{2-}	TNH_x	Na^+	Cl^-	K^+	Ca^{2+}	Mg^{2+}	RH(%)	T ($^{\circ}\text{C}$)
2012VS2011	-19.0	-1.5	4.0	-4.6	1.3	0.02	2.0	0.9	-0.2	0.04	-9.6	-5.7
2013VS2012	-4.6	-7.6	2.6	13.0	2.1	0.2	0.4	0.3	1.4	0.1	-2.6	2.1
2014VS2013	-4.5	7.9	-7.3	-14.6	-6.9	-0.4	-3.4	-1.6	-1.1	-0.2	6.6	2.0
2015VS2014	17.6	-11.2	5.2	-1.8	5.5	0.1	2.1	0.4	-0.6	0.6	-5.6	-4.2
2016VS2015	-2.3	3.0	-0.2	-4.5	-3.7	-0.03	-0.1	-0.4	0.5	-0.7	8.0	0.3
2017VS2016	-10.0	-7.2	-2.9	-5.3	-3.6	-0.2	-0.3	-0.2	-0.1	0.1	-6.0	-4.9
2018VS2017	-5.8	-0.3	-0.8	-2.4	1.3	-0.1	-0.8	-0.2	-0.1	-0.1	1.4	-2.8
2019VS2018	4.1	4.8	-3.0	-0.8	-2.2	-0.04	-0.7	-0.03	-0.1	-0.01	-0.1	7.3
2020VS2019	11.6	-3.4	4.9	-0.3	-0.9	0.1	0.1	-0.2	0.7	0.02	-6.6	-2.1
2021VS2020	-12.7	-1.5	-3.6	-2.3	0.2	-0.01	0.03	0.01	0.1	0.04	-2.8	-1.5
2022VS2021	-10.6	-1.5	-5.1	1.9	-1.4	0.03	-0.3	0.01	0.5	0.04	4.7	5.8

767

768

References

- Bi, X., Feng, Y., Wu, J., Wang, Y., and Zhu, T.: Source apportionment of PM₁₀ in six cities of northern China, *Atmospheric Environment*, 41, 903–912, <https://doi.org/10.1016/j.atmosenv.2006.09.033>, 2007.
- Chow, J.C., Watson, J.G., 1994. Guidelines for PM₁₀ sampling and analysis applicable to receptor modeling. Washington, DC: US Environmental Protection Agency, Office of Air Quality Planning and Standards, EPA-452/R-94-009.
- Gong, P. and Luo, Y.: Study on the characteristics of source profiles in Wuhan, *Journal of Nanjing University of Information Science & Technology*, 10, 579–589, <https://doi.org/10.13878/j.cnki.jnuist.2018.05.008>, 2018.
- Tremper, A.; Font, A.; Priestman, M.; Hamad, S.; Chung, T.; Pribadi, A.; Brown, R.; Goddard, S.; Grassineau, N.; Petterson, K.; Kelly, F.; Green, D.: Field and laboratory evaluation of a high time resolution x-ray fluorescence instrument for determining the elemental composition of ambient aerosols, *Atmos. Meas. Tech.*, 11, 3541–3557, <https://doi.org/10.5194/amt-11-3541-2018>, 2018.
- Wang, Y., Peng, L., Li, L., Wang, Y., Zhang, T., Liu, H., and Mu, L.: Chemical compositions and sources apportionment of re-suspended dust in Jincheng, *Environmental Science*, 37, 82–87, <https://doi.org/10.13227/j.hjlx.2016.01.012>, 2016.
- Xu, Y., Gong, X., and Zhang, W.: Construction and characteristic analysis of PM_{2.5} source profiles of typical emissions in Nanchang City, *Chemical Engineer*, 33, 41–43, <https://doi.org/10.16247/j.cnki.23-1171/tq.20190841>, 2019.
- Yang, Y.: The Chemical Compositions and Source Apportionment of Particulate matter of Open Sources in Xi'an, 42–43, <https://doi.org/10.27393/d.cnki.gxazu.2016.000073>, 2016.
- Zhang, J., Wei, E., Wu, L., Fang, X., Li, F., Yang, Z., Wang, T., and Mao, H.: Elemental composition and health risk assessment of PM₁₀ and PM_{2.5} in the roadside microenvironment in Tianjin, China, *Aerosol and Air Quality Research*, 18, 1817–1827, <https://doi.org/10.4209/aaqr.2017.10.0383>, 2017.